CHAPTER 31 ■ DIFFUSION AND DIFFUSION TENSOR MR IMAGING: FUNDAMENTALS

PETER J. BASSER

INTRODUCTION

Along with the evolution and maturation of conventional magnetic resonance imaging (MRI) methods over the last two decades, it has also become apparent that the measurement of diffusion properties in neural tissue provides unique information that has potential biological and clinical relevance. Specifically, diffusion properties of tissue constituents imply characteristics of tissue microstructure and architectural organization. Moreover, this information is obtained noninvasively and without exogenous contrast agents. Indeed, some form of diffusion MR sequencing has become routinely implemented in most clinical MRI studies evaluating cerebral tissue for the presence of disease. In a growing number of conditions affecting brain structure, more complex diffusion sequences are also being used to serve as the microanatomic correlate of disordered function in a wide range of clinical disease states. Before looking at the specific structural and architectural features that can be inferred from MR diffusion measurements, this chapter establishes the conceptual and methodologic underpinnings of diffusion nuclear magnetic resonance (NMR) and diffusion MRI.

PHYSICAL UNDERPINNINGS OF DIFFUSION NMR AND MRI

The classic macroscopic, phenomenologic picture of molecular diffusion is best exemplified by considering the behavior of molecules within a diffusion cell (Fig. 31.1). There, molecular solutions of different concentrations placed in two initially separate compartments are allowed to mix together through a permeable membrane between them. A *net* macroscopic molecular flux, **J**, can be observed as particles move from the compartment of higher concentration to that of lower concentration. Fick's first law, a phenomenologic relationship between **J** and the concentration gradient, describes this mixing process. In it, the scalar diffusion coefficient, D, appears as a scaling factor. Rapid mixing between compartments results when the diffusivity is high; slower mixing results when the diffusivity is low. A variety of tracer techniques can be used to measure diffusion coefficients from the simultaneous measurement of the flux and the concentration gradient or from concentration profiles measured as a function of time (1,2), but all such methods require either chemically or physically labeling the tracer molecules and detecting their distribution. Invasive tracer experiments have been performed to determine the diffusivity of metabolites in the brains of animals (3,4).

The discovery of Brownian motion (5) and the mathematical models describing it provided the basis of the modern picture of molecular diffusion (6,7). In the Brownian view, diffusion is a process that causes particle mixing because of random collisions among themselves (self-diffusion) or with other particles. This conceptual picture is represented schematically in Fig. 31.2 by a jagged trajectory of an individual molecule buffeted by random collisions with neighboring molecules. Unlike the deterministic picture of molecular transport implicit in Fick's law, the Brownian description is inherently a probabilistic one. Although the precise trajectory of each molecule is not known per se, their aggregate behavior—embodied in the displacement probability distribution—can still be determined. Specifically, the displacement distribution is the probability of finding a molecule at a particular position and at a particular time, given that it previously occupied another position at an earlier time. One of many fundamental contributions made by Einstein (7) to understanding the physics of diffusion was to relate the variance of this Brownian displacement distribution—the mean-squared displacement in one dimension, $\langle x^2 \rangle$—to the diffusion coefficient, D, appearing in Fick's first law and the diffusion time, τ:

$$\langle x^2 \rangle = 2D\tau \qquad [1]$$

(In three dimensions, the coefficient 2 should be replaced by 6.) Thus, the larger the diffusion coefficient, D, the greater the distance a particle is expected to travel on average during the same diffusion time.

Classic NMR measurements of (translational) molecular diffusion were based on the Brownian rather than the Fickian picture. The distinction is important because the Brownian description enables one to measure a molecular diffusion coefficient without using exogenous tracers. In essence, in the NMR measurement of diffusion, the diffusivity is inferred from the phase dispersion of the magnetization (loss in signal) caused by the assumed random displacements of molecules.

The first person to describe the effect of molecular diffusion on the NMR signal was Erwin Hahn (8). The first measurements of the self-diffusivity of water (and of other liquids) using NMR methods were reported in the earlier 1950s (9). In a series of classic experiments, Carr and Purcell used the NMR

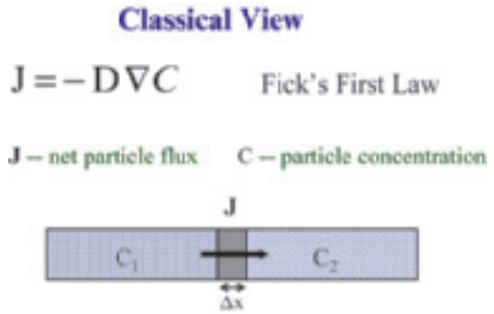

FIGURE 31.1. The Fickian picture of diffusion is best understood by considering the behavior of the diffusion cell, schematically represented here, in which the particle concentration is different in two compartments that are separated by a permeable membrane.

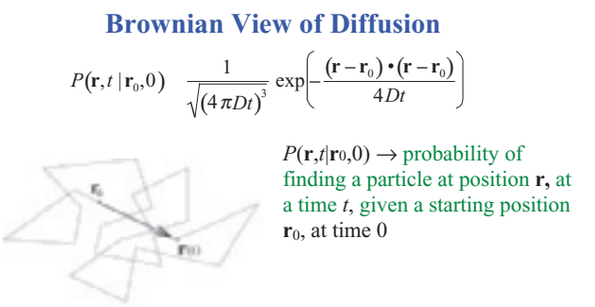

FIGURE 31.2. The Brownian picture of diffusion is best epitomized by this cartoon illustrating a possible path taken by a molecule that is released at point $\mathbf{r}_0$ at time $t = 0$ and moves to position **r** at a later time *t*. The molecule undergoes a "drunken walk" whose displacement is characterized by a probability distribution.

spin echo, also discovered by Hahn (8), to measure the self-diffusion coefficient of water and other solvents (9). Carr and Purcell first showed that the NMR spin echo could be sensitized specifically to the translational motion of a spin-labeled species by subjecting it to a static magnetic field gradient. An example of their NMR sequence is given in Fig. 31.3A. They then showed that the random motions caused by diffusion reduce the amplitude of the NMR spin echo. The larger the diffusivity of the spin-labeled molecules, the greater the phase dispersion and the larger the attenuation of the magnitude signal they observed. By using a Brownian, probabilistic description of molecular displacements of the spin system subjected to a uniform magnetic field gradient, they derived an analytic expression relating the NMR signal attenuation and the molecular diffusion coefficient. Their conceptual framework is the basis for modern diffusion MR studies. Their work also established the nonperturbing and highly accurate NMR measurement of the self-diffusion coefficient of water and other solvents as a "gold standard."

Two years later, Torrey incorporated the diffusion of magnetized spins explicitly in the Bloch (magnetization transport) equations (10), showing how it leads to additional attenuation the NMR signal (11). Analytic solutions to this equation followed for freely diffusing species during a spin echo experiment (12) and, later, for diffusion in restricted geometries (13–15).

The next key innovation in the evolution of NMR diffusion measurements was the development and use of pulsed-field gradient methods (16). By applying two appropriately placed short-duration magnetic field gradient pulses rather than one that is constant in time, the NMR diffusion experiment could be performed more accurately and with an ability to control independently the diffusion time and length scale that is probed (14). An example of a pulsed gradient sequence is shown in Fig. 31.3B. Using their new pulsed gradient sequence, Stejskal and Tanner extended the findings of Carr and Purcell, showing that uniformly translating spins produce a net phase shift that is proportional to their velocity, and that diffusing spins produce no net phase shift but a change in the height of the phase *distribution* (16). They generalized the mathematical framework of McCall et al. (17) for relating the signal attenuation, A/A_0; the conditional displacement distribution, $P(\mathbf{r}_2, \Delta|\mathbf{r}_1, 0)$; the pulse duration, δ; the pulse strength, G; the gyromagnetic ratio, γ; and the time between pulses, Δ:

$$\frac{A}{A_0} \quad \int_{-\infty}^{\infty}\int_{-\infty}^{\infty} P(\mathbf{r}_2, \Delta|\mathbf{r}_1, 0)e^{i\gamma\delta\mathbf{G}\cdot(\mathbf{r}_2-\mathbf{r}_1)}\,d^3\mathbf{r}_2\,d^3\mathbf{r}_1 \qquad [2]$$

where the assumptions are also made that δ is infinitesimally short and negligible displacements occur during the pulse period compared with during the diffusion time, that is, $\delta \ll \Delta$.

Here, $P(\mathbf{r}_1)$ is the initial distribution of spins, and $P(\mathbf{r}_2, \Delta|\mathbf{r}_1, 0)$ is the probability that a particle starting at position $\mathbf{r}_1$ at time 0 ends up at position $\mathbf{r}_2$ at time Δ.

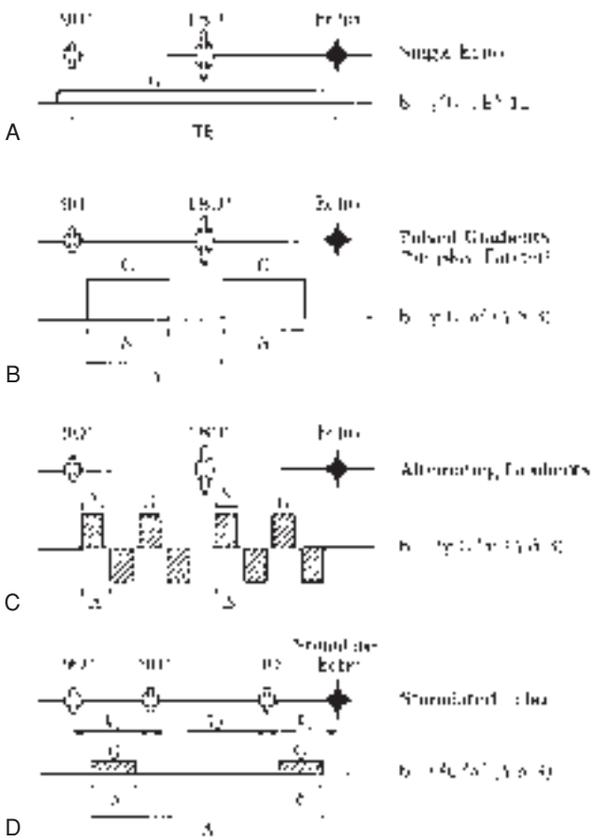

FIGURE 31.3. Several paradigmatic diffusion sequences are shown with the radiofrequency signal on the top line and the diffusion gradient pulse train on the bottom line. The corresponding *b* values (which measure the degree of diffusion weighting of the nuclear magnetic resonance signal) are given in terms of the gradient strength, G, pulse width, δ, and pulse separation, Δ. Spin echo sequences include (**A**) a constant gradient, (**B**) matched rectangular gradients, and (**C**) alternating gradients. A diffusion-weighted stimulated echo sequence is also shown (**D**). Generally, each diffusion sequence can be incorporated into virtually any magnetic resonance imaging sequence to produce a diffusion-weighted image.

This equation looks formidable, and generally it is difficult to evaluate analytically in all but the simplest of geometries (18). In the simplest case—free diffusion in an unbounded, isotropic, homogeneous medium—$P(\mathbf{r}_2, \Delta|\mathbf{r}_1, 0)$ is Gaussian:

$$P(\mathbf{r}_2, \Delta\ \mathbf{r}_1, 0) = \frac{1}{\sqrt{(4\pi D\Delta)^3}}\, e^{-\left(\frac{(\mathbf{r}_2 - \mathbf{r}_1)^2}{4D\Delta}\right)}$$

or

$$P(\mathbf{r}, \Delta\ 0, 0) = \frac{1}{\sqrt{(4\pi D\Delta)^3}}\, e^{-\left(\frac{\mathbf{r}^2}{4D\Delta}\right)} \qquad [3]$$

where D is the diffusion coefficient and $\mathbf{r}$ is the net displacement, $\mathbf{r} = \mathbf{r}_2 - \mathbf{r}_1$. If we also assume that the initial distribution of spins, $P(\mathbf{r}_1)$, is uniform, then substituting the second expression of Eq. 3 into Eq. 2 yields

$$\frac{A(\gamma\delta G)}{A_0} = \frac{A(q)}{A_0} = \int_{-\infty}^{\infty} \frac{1}{\sqrt{(4\pi D\Delta)^3}}\, e^{-\left(\frac{r^2}{4D\Delta}\right)} e^{iqr}\, d^3r, \qquad [4]$$

$$\text{where} \quad |\mathbf{r}| = r \quad \text{and} \quad q = \frac{1}{2\pi}\,\gamma\delta G$$

This integral is a three-dimensional (3D) Fourier transform of a Gaussian displacement distribution with respect to q, defined here. Evaluating Eq. 4 also results in a Gaussian distribution of the form

$$\frac{A}{A_0} = e^{-q^2 D\Delta} \quad \text{or} \quad \ln\left(\frac{A}{A_0}\right) = -q^2 D\Delta \qquad [5]$$

This simple expression in Eq. 5 highlights how variations in the spatial scale parameter, q, and the diffusion time, Δ, independently affect the signal attenuation. In a medium in which water does not move freely—in which it is confined within internal compartments (restricted), is reflected by obstacles but still free to meander relatively freely throughout the medium (hindered), or experiences higher diffusivity in some directions and lower in others (anisotropic)—this simple relationship no longer holds. Still, the approach used to derive Eq. 5 can be generalized to treat each of these more complex cases (e.g., ref. 18).

Tanner later proposed the stimulated echo sequence and discovered that it could also be sensitized to the effects of molecular diffusion (19). This sequence is shown in Fig. 31.3D. In spin echo NMR diffusion experiments, the net magnetization remains in the transverse plane for the duration where spins dephase with a time constant T_2. In most tissues, however, T_2 is short (on the order of 10 to 100 ms) compared to T_1. For diffusion times greater than T_2, the loss of signal due to T_2 relaxation then limits the possibility of observing the additional signal attenuation caused by the application of diffusion gradients within the sequence. The stimulated echo sequence addresses this problem by storing the magnetization in the longitudinal direction for a prescribed period (the mixing time). Although this trick reduces T_2 signal loss and extends the maximum diffusion time of the sequence, the price one pays is the reduction in signal intensity by a factor of two compared with the spin echo sequence.

Tanner also recognized that when NMR methods are used to measure water diffusion in complex media, one must abandon the notion of the self-diffusivity or self-diffusion constant. In its place, he proposed an "apparent diffusion coefficient" (20), which has come to be referred to as an ADC. The ADC is usually defined as the ratio of the mean-squared displacement to twice the diffusion time. Generally, it is sensitive to the composition and ultra and microstructure of the material in which the molecules are diffusing, as well as interactions between the diffusing molecule and other molecular constituents in the medium.

Tanner also introduced the notion of the scalar "b factor" to relate the ADC to the NMR signal attenuation, $A(b)/A(0)$:

$$\ln\left(\frac{A(b)}{A(0)}\right) = -b\ \text{ADC} \qquad [6]$$

where $A(b)$ is the measured echo magnitude; b is a measure of the degree of diffusion weighting and depends on the strength of the diffusion gradient pulses and the timing diagram, such as the pulse width and temporal separation (20); and $A(0)$ is the echo magnitude without diffusion gradients applied. This relationship is used in most modern diffusion MR studies, with some notable modifications.

Figure 31.3 also shows the relationship between the NMR pulse sequence parameters for a family of pulse sequences commonly used in diffusion NMR studies. These include (a) a constant gradient, (b) matched rectangular gradient pulses, and (c) a train of bipolar gradients. These pulsed gradients are typically incorporated in spin echo or stimulated echo sequences; however, diffusion sensitization can also be achieved by applying them as diffusion preparation pulses prior to the application of an imaging sequence. Nevertheless, the b factor formalism is quite general and, in principle, can be used for any pulse sequence. Refinements and corrections to these formulas for nonrectangular pulses have also been calculated (21).

In diffusion NMR, a single scalar diffusion coefficient or ADC is measured from a set of diffusion-weighted signals, generally by using linear regression of Eq. 6. Diffusion coefficients are generally obtained by systematically varying b, by varying either G or Δ or both, and then measuring the slope of the semilogarithmic plot of $\ln[A(b)/A(0)]$ versus b (16).

The application of this measurement of water diffusion properties in tissues by NMR methods to tissues has a surprisingly long history (22). Pioneering studies by Chang et al. (23,24), Rorschach et al. (25), Cooper et al. (26), Hazlewood et al. (27), and Tanner (19,20,28,29), and by Cleveland et al. (30) and Hansen (31) in skeletal muscle and Hansen (31) in brain tissue, all significantly pre-date the earliest diffusion MRI studies of these and other tissues (32–35) by well more than a decade. Even anisotropic diffusion was detected in NMR experiments on skeletal muscle (36).

These early NMR studies measured the diffusion of protons in tissue because water is so abundant there (approximately 100 molar), and the large gyromagnetic ratio of protons in water results in a large measurable NMR signal. It was also clear to these investigators why this NMR methodology is well suited to the study of cells and tissues—for typical diffusion times, the NMR diffusion experiment can probe water displacements at micrometer length scales. This can be seen from the Einstein equation, Eq. 1. Assuming that for free water at 37°C, $D \sim 3 \times 10^3\ \mu m^2/s$ and the diffusion time is on the order of 0.02 second, one finds that the root mean-squared (RMS) displacement is about 10 μm, which is comparable to a cell diameter.

Diffusion Imaging

The development of MRI entailed using NMR pulse gradient sequences specifically to localize a population of spins in space (37). As Lauterbur perspicaciously observed, it also created the potential for incorporating existing NMR measurements of relaxation properties within an MRI sequence: "The basic zeugmatographic principle . . . permits the generation of two

and three dimensional images displaying chemical compositions, diffusion coefficients, and other properties of objects measurable by spectroscopic techniques" (37). Although the possibility of combining diffusion NMR and MRI was foreseen by Lauterbur in 1973 (37), it was not until 1984 that diffusion MRI was first realized. In a series of two papers, Wesbey et al. showed how one can account for the effects of diffusion gradients within an MRI sequence (35) and demonstrated diffusion MRI in different phantoms (34). Unfortunately, this implementation of diffusion MRI (DI) did not allow for separate control of the imaging gradients used to perform spatial localization and of the diffusion gradients used to sensitize the mobile spins to be able to measure their displacements. However, in 1985, clinically useable diffusion MRI sequences were first proposed and realized (22,32,33) that overcame this problem. Several excellent books and review articles have been written describing many important aspects of diffusion MRI (e.g., refs. 38 and 39).

Diffusion-Weighted Images

Diffusion weighted images (DWIs) are MRIs obtained by incorporating diffusion gradient pulses within a conventional MRI pulse sequence (34). The intensity of a DWI is "weighted" or attenuated by the effective diffusivity of the spin-labeled species in each voxel, just as the diffusion NMR signal is weighted or attenuated by the diffusivity within the excited volume. Technical issues associated with the acquisition and analysis of DWIs are discussed later.

Diffusion Imaging and Apparent Diffusion Coefficient Maps

Just as a scalar diffusivity can be measured from a series of diffusion-weighted NMR spin echoes, a scalar ADC in each voxel can be measured from a set of DWIs. These images are generally referred to as ADC maps. Specifically, from these DWIs, an ADC is estimated in each voxel using linear regression of Eq. 6, just as a single ADC in a diffusion NMR experiment is estimated. An important innovation in DI, however, is that the b value (20) in general must include not only the effects of the diffusion gradients themselves, but also those of the imaging gradients (38). Originally, it was thought that only imaging gradients applied along the same direction as the diffusion-sensitizing gradient direction needed to be included in the evaluation of the b factor (38,40), but it was shown that imaging gradients applied in other directions may produce additional diffusion weighting (41). This common misconception was probably based on statements made in earlier diffusion NMR studies (16,19).

DI is inherently a *one-dimensional* technique, that is, we can use it to measure the projection of all molecular displacements along only one direction. In tissues such as brain gray matter in which the ADC is largely independent of the orientation of the tissue (isotropic), acquiring such information is usually sufficient. However, in anisotropic media such as skeletal and cardiac muscle (29,30,42) and in white matter (43–46) in which the ADC is known to depend on the orientation of the tissue, no single ADC can characterize the orientation-dependent water mobility in these tissues. Such orientationally biased diffusion, however, can be characterized more faithfully by a symmetric effective or apparent diffusion *tensor* of water, $\underline{D}$ (e.g., ref. 1). The NMR measurement of $\underline{D}$ (47) and the analysis and display of the information it contains in each voxel is called diffusion tensor imaging (DTI) or diffusion tensor MRI (also called DTI) (48).

DIFFUSION TENSOR MRI

Diffusion tensor MRI (sometimes abbreviated as DT-MRI but more commonly as DTI) is inherently *three dimensional*. In DTI, the effective diffusion tensor, $\underline{D}$ (or functions of it), is estimated from a series of DWIs using a relationship between the measured echo signal in each voxel and the applied magnetic field gradient sequence (47,49–51) that is based on Stejskal's solution to the modified Torrey-Bloch equation (16):

$$\ln\left(\frac{A(\underline{b})}{A(\underline{b}=\underline{0})}\right) = -\sum_{i}^{3}\sum_{j}^{3} b_{ij}D_{ij} = -(b_{xx}D_{xx} + 2b_{xy}D_{xy} + 2b_{xz}D_{xz} + b_{yy}D_{yy} + 2b_{yx}D_{yx} + b_{zz}D_{zz}) \quad [7]$$

Here, $A(\underline{b})$ is the echo magnitude of the diffusion-weighted signal, $A(\underline{b} = \underline{0})$ is the echo magnitude of the non–diffusion-weighted signal, and bij is a component of the symmetric b matrix, $\underline{b}$. Just as in DI, in which a scalar b factor is calculated for each DWI, in DTI a symmetric b matrix is calculated for each DWI. Whereas the b value summarizes the attenuating effect on the MR signal of diffusion and imaging gradients in one direction (40), the b matrix summarizes the attenuating effect of all gradient waveforms (i.e., all imaging and diffusion gradient sequences) applied in all three directions, x, y, and z (47,49–51). Just as in DI one uses each DWI and its corresponding b factor to estimate an ADC using linear regression of Eq. 6, in DTI one uses each DWI and its corresponding b matrix to estimate $\underline{D}$ using multivariate linear regression[1] of Eq. 7.

There are two important distinctions between DI and DTI. In DTI one must apply diffusion gradients along at least six noncollinear directions (47), whereas in DI it is sufficient to apply diffusion gradients along only one direction. Second, one must expand the notion of "cross-terms" between imaging and diffusion gradients to account for possible interactions between imaging and diffusion gradients that are applied in orthogonal directions and even between imaging gradients that are applied in nonorthogonal directions (49,50). In isotropic media, gradients applied in orthogonal directions do not produce cross-terms, but in anisotropic media, they can. This fact had not been considered before.

Finally, it is easy to see that DTI subsumes DI. If the medium is isotropic, then $D_{xx} = D_{yy} = D_{zz} = D$ and $D_{xy} = D_{xz} = D_{yz} = 0$. Then Eq. 7 reduces to Eq. 6 with $b = b_{xx} + b_{yy} + b_{zz} = \mathrm{Trace}(\underline{b})$. If the medium is not isotropic, then one can show that ADC, D, measured along a direction specified by the unit column vector $\hat{\mathbf{r}}$ is given by $\hat{\mathbf{r}}^T\,\underline{D}\,\hat{\mathbf{r}}$.

It is important to note that MRI measurements of the ADC, T_1, T_2, magnetization transfer rate, proton density, and chemical spectra were all preceded by classical NMR measurements of these quantities, which in some cases were first performed almost a half century before their MRI counterpart was. This was not the case with DTI. There were no classical NMR methods developed to measure the self-diffusion tensor or the effective (or apparent) diffusion tensor of water (or other media) in an arbitrary laboratory coordinate system. Thus, the development of DTI (48) first required the invention of a methodology to measure $\underline{D}$ from the NMR signal (47,52).

[1]Multivariate linear regression is just one of a number of techniques, including nonlinear regression and singular-value decomposition, that could be used to estimate $\underline{D}$ from the echo data.

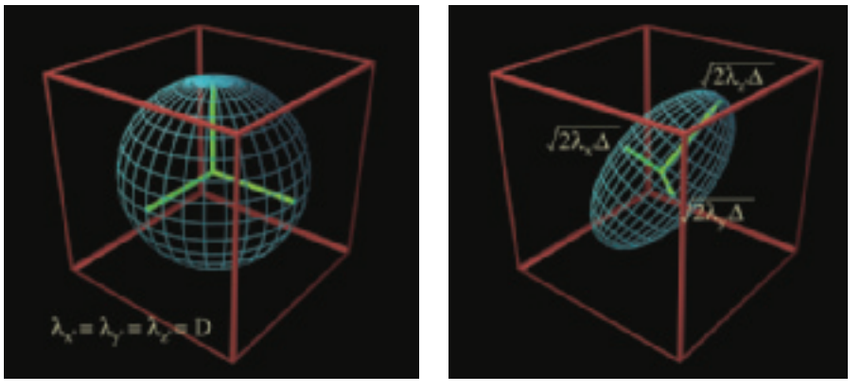

A B

FIGURE 31.4. A: In isotropic media, the root-mean-squared displacement or diffusion ellipsoid is spherical. **B:** However, in anisotropic media, the diffusion ellipsoid is either prolate or oblate, and its three principal directions are coincident with the eigenvectors of $\underline{D}$, namely λ_1, λ_2, and λ_3.

Geometric Representation of Translational Diffusion in Three Dimensions

The simplest and most intuitive way to understand the information content in $\underline{D}$ is by considering a *Gedanken* experiment in which we follow the Brownian motion of an ensemble of "tagged" water molecules released from the center of a voxel. If the rate of diffusive transport is the same in all directions, diffusion is said to be isotropic and is completely specified by a single scalar constant, D, the diffusion coefficient. Thus, diffusion isotropy describes the case in which the molecular diffusivity is independent of the medium's orientation, so the corresponding diffusion tensor in this case is an isotropic tensor (53). For a diffusion time, Δ the translational displacement distribution is spherically symmetric, and surfaces of constant probability or water concentration are concentric spheres, as seen by setting the exponent of Eq. 3 to a constant. It is convenient to choose the constant to be 1/2; then

$$<r^2> = (\sqrt{2D\Delta})^2 = 2D\Delta \qquad [8]$$

where the radius of the diffusion sphere, $\sqrt{2D\Delta}$, is one half of the standard deviation, σ, of $P(\mathbf{r}, \Delta|\mathbf{0}, 0)$:

$$\sigma = \sqrt{4D\Delta} \qquad [9]$$

Using the well-known Einstein formula (7) as given in Eq. 8, we see that the radius of this particular diffusion sphere equals the RMS displacement of water molecules after diffusion time Δ. A graphical representation of this diffusion sphere is shown in Fig. 31.4A.

Diffusion anisotropy implies that the translational displacement of the diffusing species depends on the medium's orientation. In homogeneous anisotropic media, the voxel-averaged displacement distribution is slightly more complicated than Eq. 3:

$$P(\mathbf{r}, \Delta|\mathbf{0}, 0) = P((x, y, z), \Delta|(0, 0, 0), 0) \qquad [10]$$

$$\frac{1}{\sqrt{|\underline{D}|\,(4\pi\Delta)^3}} \exp\left(\frac{-(x, y, z)\,\underline{D}^{-1}\,(x, y, z)^T}{4\Delta}\right)$$

Now the matrix of variances and covariances, $2\Delta\underline{D}$, in Eq. 10, replaces the variance, $2\Delta D$, in Eq. 3; the $|\underline{D}|$ that appears in Eq. 10 replaces D^3 in the normalization factor of $P(\mathbf{r}, \Delta|\mathbf{0}, 0)$ in Eq. 3. So, when we construct surfaces of constant probability [again by setting the exponent of $P(\mathbf{r}, \Delta|\mathbf{0}, 0)$ to a constant], we obtain

$$(D_{yy}D_{zz} - D_{yz}^2)\,x^2 + 2(D_{xz}D_{yz} - D_{xy}D_{zz})xy + (D_{xx}D_{zz} - D_{xz}^2)y^2 + 2(D_{xy}D_{yz} - D_{xz}D_{yy})xz + 2(D_{xy}D_{xz} - D_{xx}D_{yz})yz + (D_{xx}D_{yy} - D_{xy}^2)z^2 = |\underline{D}|\Delta \qquad [11a]$$

which, when written more compactly as

$$ax^2 + 2bxy + dy^2 + 2cxz + 2eyz + fz^2 = 1 \qquad [11b]$$

is easily recognized as the equation of a three-dimensional ellipsoid[2] called the "diffusion ellipsoid" (1,14,48). There is an interesting connection between this geometric construct,[3] which is depicted in Fig. 31.4B, and the three-dimensional displacement distribution: In general, six free parameters are required to specify the shape and orientation of the ellipsoid and the number of independent components of the diffusion tensor required to specify the form of the three-dimensional displacement distribution for some diffusion time Δ. In a fully anisotropic medium, all six independent parameters (*a, b, c, d, e, f*) in Eq. 11b, or equivalently all six independent coefficients of $\underline{D}$ (D_{xx}, D_{yy}, D_{zz}, D_{xy}, D_{xz}, and D_{yz}) are required; in a cylindrically symmetric (transversely isotropic) medium, four independent parameters in Eq. 11b, or equivalently four independent components of $\underline{D}$, are required, whereas in an isotropic medium, only one parameter, D, is required (54, 55).

For an anisotropic medium, we can always rotate our laboratory (x, y, z) coordinate axes so that they are aligned with the local principal (x′, y′, z′) axes of the diffusion ellipsoid in each voxel. In this frame, all off-diagonal elements of $\underline{D}$ vanish, and the equation describing the diffusion ellipsoid, Eq. 11a, simplifies to

$$\left(\frac{x'}{\sqrt{2\lambda_{x'}\Delta}}\right)^2 + \left(\frac{y'}{\sqrt{2\lambda_{y'}\Delta}}\right)^2 + \left(\frac{z'}{\sqrt{2\lambda_{z'}\Delta}}\right)^2 = 1 \qquad [12]$$

Here $\lambda_{x'}$, $\lambda_{y'}$, and $\lambda_{z'}$ are the principal diffusivities (or eigenvalues) along the three respective principal directions $\varepsilon_{x'}$, $\varepsilon_{y'}$, and $\varepsilon_{z'}$, and $\sqrt{2\lambda_{x'}\Delta}$, $\sqrt{2\lambda_{y'}\Delta}$, and $\sqrt{2\lambda_{z'}\Delta}$, are the RMS displacements along these three principal directions at time Δ, respectively. The lengths of the major and minor axes of the diffusion ellipsoid represent these three distances geometrically. It is important to note that the direction of the principal (x′, y′, z′) axes of the diffusion ellipsoid are usually not known a priori and generally do not coincide with the (x, y, z) laboratory coordinate axes. Moreover, the orientation of the ellipsoid must be assumed to change in each voxel and thus must be determined experimentally in each voxel (47).

In summary, both diagonal and off-diagonal elements of $\underline{D}$ are essential in specifying the probability distribution in Eq. 10 as well as in characterizing the *size*, *shape*, and

[2]This is true because both $\underline{D}$ and the coefficient matrix are positive definite.

[3]We distinguish between the "measurement" and "diffusion" ellipsoids, which are related to each other through a 3D Fourier transform.

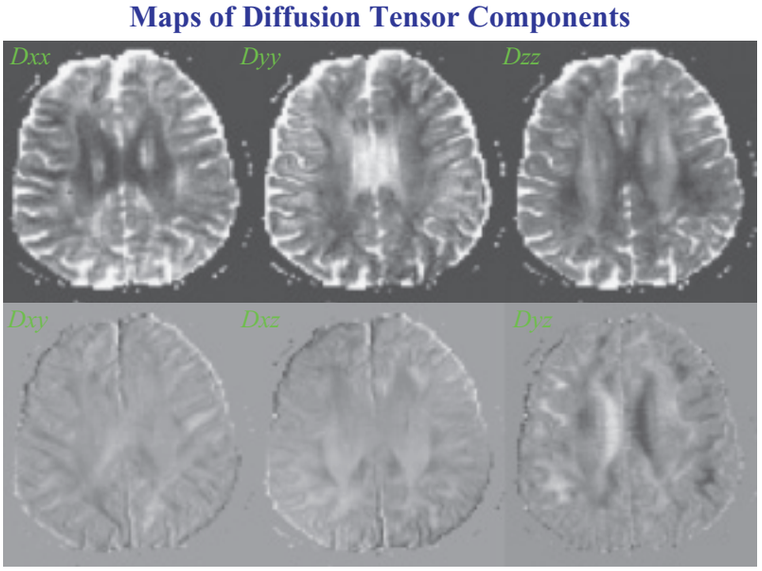

FIGURE 31.5. Diffusion tensor magnetic resonance imaging provides data for each slice within the imaging volume that consist of images of the three diagonal elements of $\underline{D}$ (**top row**) and of the three off-diagonal elements of $\underline{D}$ (**bottom row**). (From Pierpaoli C, Jezzard P, Basser PJ, et al. Diffusion tensor MR imaging of the human brain. *Radiology* 1996;201(3):637–648, with permission.)

orientation of the diffusion ellipsoid constructed from $\underline{D}$ in each voxel (Fig. 31.5). Diagonal and off-diagonal elements of $\underline{D}$ are also used to calculate the MRI parameters discussed later.

Quantitative DTI

Using information gleaned from the *size*, *shape*, *orientation*, and *distribution* or *spatial pattern* of diffusion ellipsoids within an imaging volume, we can characterize new features of water diffusion within a voxel. The diffusion ellipsoid image characterizes much of this information. It consists of a diffusion ellipsoid displayed in each voxel, which is calculated from the measured diffusion tensor there. An example of an *in vivo* diffusion ellipsoid image is shown in Fig. 31.6.

Scalar parameters that embody the distinct intrinsic features listed in the previous paragraph in italics are typically calculated from the diagonal *and* off-diagonal elements of $\underline{D}$ and can also be displayed as an image. The parameters describing the size and shape of the ellipsoid should be rotationally invariant, that is, independent of the orientation of the tissue structures, the patient's body within the MR magnet, the applied diffusion-sensitizing gradients, and the choice of the laboratory coordinate system in which the components of the diffusion tensor and magnet field gradients are measured (56,57).

The most important quantitative scalar parameters provided by DTI are the three sorted eigenvalues (i.e., the eigenvalues of $\underline{D}$ described earlier but sorted in size order) λ_1, λ_2, and λ_3, which are useful in characterizing the size and shape of the diffusion ellipsoid. An example of an eigenvalue image is shown in Fig. 31.7.

In particular, the three fundamental scalar invariants of $\underline{D}$, I_1, I_2, and I_3, are defined explicitly as functions of $\underline{D}$:

$$I_1 = \lambda_1 + \lambda_2 + \lambda_3 = \text{Trace}(\underline{D})$$

$$I_2 = \lambda_1\lambda_2 + \lambda_2\lambda_3 + \lambda_1\lambda_3 = 1/2\,[\text{Trace}(\underline{D})^2 - \text{Trace}(\underline{D}^2)] \quad [13]$$

$$I_3 = \lambda_1\lambda_2\lambda_3 = \text{Det}(\underline{D})$$

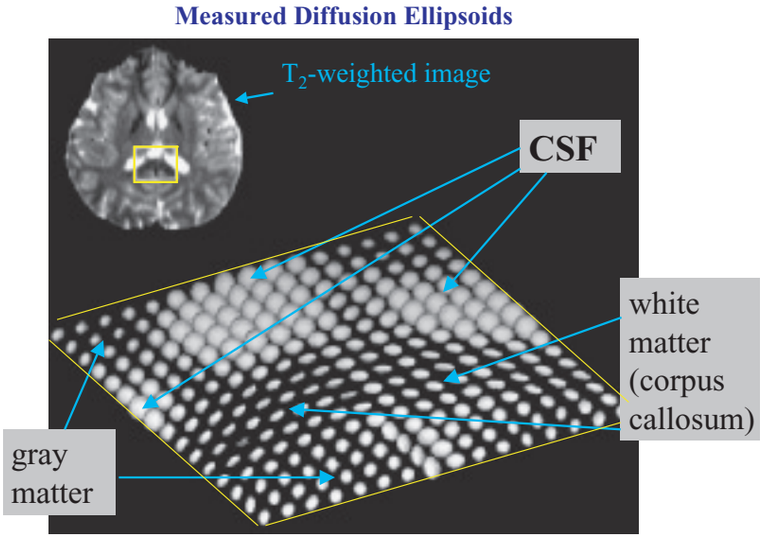

FIGURE 31.6. The T_2-weighted axial image contains a region of interest (ROI) encompassing the lateral ventricles and the corpus callosum. A diffusion ellipsoid image constructed from each voxel within the ROI shows the size, shape, and orientation of the diffusion ellipsoid. Cerebrospinal fluid (CSF) is clearly depicted by large spherical ellipsoids in which diffusion is free and isotropic. Gray matter is depicted by smaller spherical ellipsoids, indicating isotropic but lower mean diffusivity than in the CSF. White matter is depicted by prolate diffusion ellipsoids whose polar axis is aligned with the purported white matter fiber direction in the corpus callosum. (From Pierpaoli C, Jezzard P, Basser PJ, et al. Diffusion tensor MR imaging of the human brain. *Radiology* 1996;201(3): 637–648, with permission.)

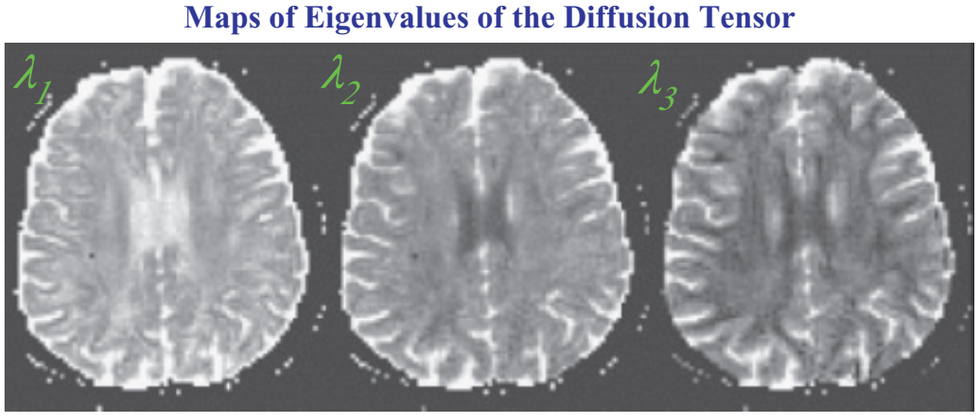

FIGURE 31.7. Images or maps of the three sorted eigenvalues λ_1, λ_2, and λ_3. Different regions of brain can be distinguished by examining these images. Cerebrospinal fluid is uniformly bright in these images, indicating that diffusion is isotropic and high there. Gray matter regions are nearly uniform in brightness, whereas white matter regions, like the corpus collosum at the center, is bright in the λ_1 image but dark in the λ_2 and λ_3 images, indicating significant diffusion anisotropy there. (From Pierpaoli C, Jezzard P, Basser et al. Diffusion tensor MR imaging of the human brain. *Radiology* 1996;201(3):637–648, with permission.)

I_1, I_2, and I_3 also appear as coefficients of the characteristic equation of $\underline{D}$,

$$\lambda^3 - I_1\lambda^3 + I_2\lambda - I_3 = 0 \qquad [14]$$

which is used to calculate λ_1, λ_2, and λ_3.

Another desirable property of the scalar invariants and their functions is that each is independent of the order of the eigenvalues; therefore, their value is unchanged when we permute the subscripts of the eigenvalues. Moreover, each scalar invariant has a distinct geometrical (and physical) interpretation. I_1 is proportional to the sum of the squares of the major and minor axes of the diffusion ellipsoid. I_2 is proportional to the sum of the squares of the areas of the three principal ellipses of the diffusion ellipsoid. I_3 is proportional to the square of the volume of the diffusion ellipsoid.

Characterizing the Size of the Diffusion Ellipsoid

The quantities to be described characterize the size of the diffusion ellipsoid, independent of its orientation and shape. The first scalar invariant, I_1, can be written in several ways:

$$\begin{aligned} I_1 &= \text{Trace}(\underline{D}) = D_{xx} + D_{yy} + D_{zz} \\ &= 3\langle D\rangle = \lambda_1 + \lambda_2 + \lambda_3 = 3\langle\lambda\rangle \end{aligned} \qquad [15]$$

Physically, Trace($\underline{D}$) is three times the orientationally averaged diffusivity, $\langle D\rangle$, which can be obtained by arithmetically averaging the ADC uniformly over all possible directions (58). By integrating over all directions, this quantity measures an intrinsic property of the tissue, which is independent of fiber orientation, gradient directions, and so on. An example of an image of Trace($\underline{D}$) of brain parenchyma is provided in Fig. 31.8.

Moseley et al. discovered in animals (59–61), and Warach et al. later showed in humans (62,63), that a reduction of the ADC in brain parenchyma is a sensitive indicator of the onset and severity of a cerebral ischemic event. Moreover, an elevation in ADC was observed in chronic stroke, primarily in lacunar infarcts. Thus, the proposal was made to attempt to follow an acute stroke in progress and the subsequent chronic degeneration it caused. Achieving this goal was hampered by orientationally dependent diffusion characteristics of white matter as measured in DI. In anisotropic white matter, DWI intensity and the ADC depend on the direction of the diffusion-sensitizing gradient and the white matter fiber tracts in that voxel (44,64,65). Thus, it was not known whether an observed change in signal intensity is of a physiologic origin (brought on by the ischemic event itself) or arose because of the particular relative orientation of the white matter tracts and the applied diffusion gradient. In ischemia monitoring, diffusion anisotropy in white matter produced directionally dependent intensity variations in DWIs and even in ADC maps that complicated their interpretation. The solution to this problem was provided by DTI. Unlike the DWI signal intensity and the ADC, we know a priori that Trace($\underline{D}$) is inherently independent of *both* the direction of the diffusion-sensitizing gradient and the white matter fiber tract orientation in a voxel (56). Thus, Trace($\underline{D}$) eliminates all orientational dependence seen in DWIs and ADCs, and so changes in signal intensity or contrast can be ascribed solely to changes in the structure and state of the tissue. This is one factor that has contributed to the utility of Trace($\underline{D}$) in stroke assessment and monitoring. A second factor is the finding that in the mammalian brain Trace($\underline{D}$) is highly uniform in normal brain parenchyma (66–69). Remarkably, it has virtually the same value in both white and gray matter. Van Gelderen et al. (69) demonstrated experimentally in cats and Ulug et al. (68) in humans that an image of Trace($\underline{D}$) (or of $\langle D\rangle$) defines ischemic regions better than a corresponding DWI or an ADC map.

Several imaginative MR sequences have been devised to measure Trace($\underline{D}$) using only two DWIs (70–72). An image constructed from a Trace($\underline{D}$) map that is used in the assessment of stroke is a trace-weighted or isotropically weighted DWI. This can be obtained by computing Trace($\underline{D}$) and then generating an image whose intensity is a function of it, such as $\eta \exp[(-b\ \text{Trace}(\underline{D})]$, where η is a positive constant. In this image, ischemic regions appear bright and normal parenchyma appears dark.

Characterizing the Shape of the Diffusion Ellipsoid

Characterizing the degree of diffusion anisotropy is tantamount to characterizing the shape of a three-dimensional diffusion ellipsoid independent of its orientation and size. Such a

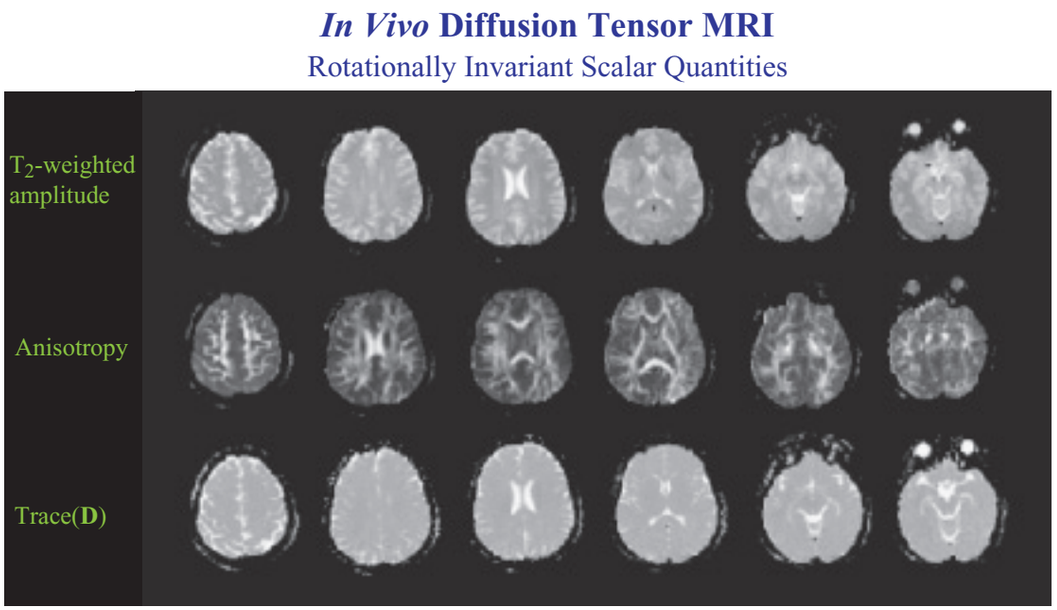

FIGURE 31.8. T_2-weighted amplitude images (**top row**) are juxtaposed with lattice anisotropy maps (**middle row**) and Trace(D) maps (**bottom row**) obtained for the same slice. Anisotropy maps highlight the white matter regions and show low or no intensity in gray matter and cerebrospinal fluid. Trace(D) images are quite uniform in normal brain parenchyma. Hyperintense regions correspond to cerebrospinal fluid or fluid-filled regions. (From Pierpaoli C, Jezzard P, Basser PJ, et al. Diffusion tensor MR imaging of the human brain. *Radiology* 1996;201(3):637–648, with permission.)

measure should also be independent of the sample's placement or its orientation with respect to the (laboratory) x, y, z reference frame (48). Arriving at such parameters is best done by analyzing the anisotropic part of the diffusion tensor or the "diffusion deviation tensor" in each voxel, $\underline{D}$ (41,73):

$$\underline{D} = \underline{\mathrm{D}} - \langle D \rangle \underline{\mathrm{I}} \qquad [16]$$

where we see the familiar mean diffusivity, $\langle D \rangle$, multiplied by the identity tensor, $\underline{I}$. The magnitude of diffusion deviation tensor, Trace($\underline{D}^2$), can be shown to be proportional to the mean-squared deviation of the eigenvalues or principal diffusivities (41):

$$1/3\ \mathrm{Trace}(\underline{D}^2) = \frac{1}{3}\left((\lambda_1 - \langle\lambda\rangle)^2 + (\lambda_2 - \langle\lambda\rangle)^2 + (\lambda_3 - \langle\lambda\rangle)^2\right)$$
$$= \mathrm{Variance}(\lambda) \qquad [17]$$

This quantity, which is rotationally invariant, is the basis of a number of diffusion anisotropy measures, such as the relative anisotropy (RA) and the fractional anisotropy (FA) (41), which both characterize the degree of "out-of-roundness" of the diffusion ellipsoid. The *RA* is just the coefficient of variation of the eigenvalues, which has been previously used in crystallography as an "aspherism coefficient" (74).

Another useful "shape" parameter is the third moment or skewness of the eigenvalues:

$$1/3\ \mathrm{Trace}(\underline{D}^3) = \frac{1}{3}\left((\lambda_1 - \langle\lambda\rangle)^3 + (\lambda_2 - \langle\lambda\rangle)^3 + (\lambda_3 - \langle\lambda\rangle)^3\right)$$
$$= \mathrm{Skewness}(\lambda) \qquad [18]$$

It helps us to decide whether the diffusion ellipsoid is prolate [i.e., cigar shaped, as observed in white matter fibers in the corpus callosum and in the pyramidal tract in monkeys (66) and in humans (67)], or oblate [i.e., pancake shaped, as observed in white matter in the subcortical white matter regions in the centrum semiovale in humans (67)]. Clearly, it would be useful to know higher moments of the distribution of eigenvalues of D, such as the Kurtosis(λ), to characterize diffusion anisotropy more completely, but background noise in DWIs can make such measured quantities unreliable. Background noise even causes one to overestimate the variance of the aforementioned eigenvalues and other measures of diffusion anisotropy (66). Pierpaoli et al. attempted to ameliorate this problem by proposing the lattice anisotropy index (67), an image of which is displayed in Fig. 31.8.

Other anisotropy measures have also been proposed, some differing from the FA and RA by only a scale factor (75). Novel measures have been proposed that are based on a "barycentric" representation of the diffusion tensor, in which it is decomposed into linelike, planelike, and spherelike tensors that correspond to diffusion ellipsoids that are prolate, oblate, and spherical, respectively (76). The information provided by this interesting approach should still be compared with the information contained in the three moments of D—the mean, variance, and skewness. One issue that should be examined in the barycentric representation of diffusion tensor data is whether it is sensitive to the order in which the eigenvalues of D are sorted. Although the moments of D given in the foregoing are insensitive to the order of the eigenvalues, dependence on their order renders quantities susceptible to a statistical bias caused when these eigenvalues are sorted (66).

Characterizing the Orientation and Directional Pattern of Diffusion Ellipsoids

Another important development in DTI is the introduction of quantities that reveal *architectural* features of anisotropic structures, such as nerve fiber tracts in brain. Useful information can be gleaned from the diffusion tensor field, which

Displaying 3-D Fibers in 2-D

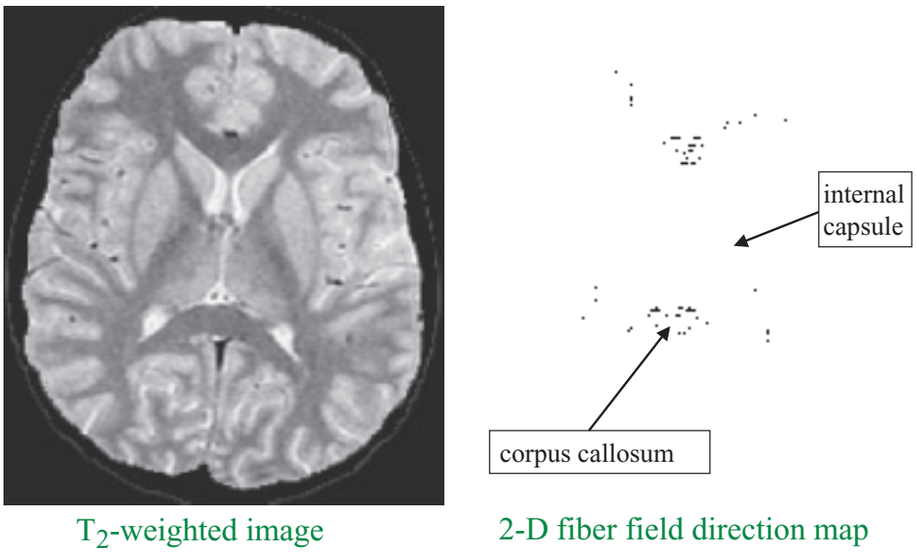

FIGURE 31.9. A T_2-weighted image juxtaposed with a two-dimensional fiber direction map of the same slice. Whereas fibers lying within the plane of the image, such as the corpus callosum, are well depicted, fibers running perpendicular to the plane of the image, such as in the internal capsule, are difficult to discern. (From Pajevic S, Pierpaoli C. Color schemes to represent the orientation of anisotropic tissues from diffusion tensor data: application to white matter fiber tract mapping in the human brain. *Magn Reson Med* 1999;42(3):526–540, with permission.)

includes the *directional pattern* of diffusion ellipsoids within an imaging volume. Early on, it was proposed that in ordered fibrous tissues, the eigenvector associated with the largest eigenvalue within a voxel is parallel to the local fiber direction (48). Imaging methods that apply this idea include direction field mapping, in which the local fiber direction is displayed as a vector in each voxel (Fig. 31.9), and fiber-tract color mapping, in which a color assigned to a voxel containing anisotropic tissue is used to signify the local fiber tract direction (Fig. 31.10) (77). A color map displaying commissural, association, and projection fibers is shown in Fig. 31.11.

DTI fiber tractography (78–88) is a DTI-based methodology for following fiber tract trajectories within the brain and other fibrous tissues. In one embodiment, fiber tract trajectories are generated from the fiber tract direction field in much the same way that fluid streamlines are generated from a fluid velocity field. Figure 31.12 shows a schematic diagram outlining how such fiber tracts are calculated from DTI data. Several examples of computed tracts in the brain are presented in Figs. 13 to 15. Streamline-based methods have been criticized for not being able to follow tracts through regions in which fiber topology is complex, that is, where fibers cross, merge, kiss, and so on. More recently, probabilistic methods have been proposed to track anatomic connections between one region of the brain and another (89,90) (Fig. 31.16). It is difficult to validate the predictions of any of these tractography methods. Certainly, unexpected artifacts in tractography can arise when discrete, coarsely sampled, noisy, voxel-averaged direction field data (81) are used or when one attempts to follow incoherently organized nerve pathways (91). These artifacts could suggest phantom connections between different brain regions that do not exist anatomically or cause the failure to elucidate connections that do exist. Moreover, the fundamental limitation in most advanced MR techniques, all of which are signal-to-noise starved, is simply inadequate signal-to-noise ratio (SNR). This basic, yet extremely important concept is often ignored by radiologists and referring doctors when presented with DTI tractography images, yet probably the most common cause of absent connectivity implied by DTI tractography is insufficient SNR (Fig. 31.17). Therefore, great care must be exercised both in obtaining and in interpreting such "connectivity" data (83).

Color Encoding of Fiber Direction

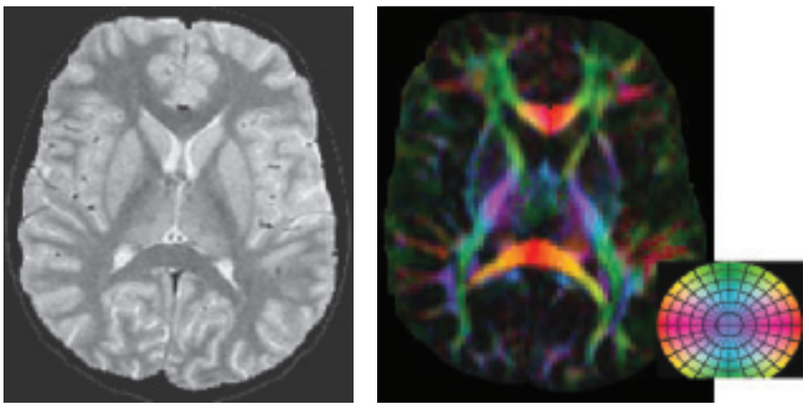

FIGURE 31.10. A T_2-weighted image juxtaposed with a direction-encoded color map of the same slice as depicted in Fig. 31.9. This color scheme overcomes the problem described in Fig. 31.9 because all fibers can be perceived and their orientations determined from the color wheel in the legend. (From Pajevic S, Pierpaoli C. Color schemes to represent the orientation of anisotropic tissues from diffusion tensor data: application to white matter fiber tract mapping in the human brain. *Magn Reson Med* 1999; 42(3):526–540, with permission.)

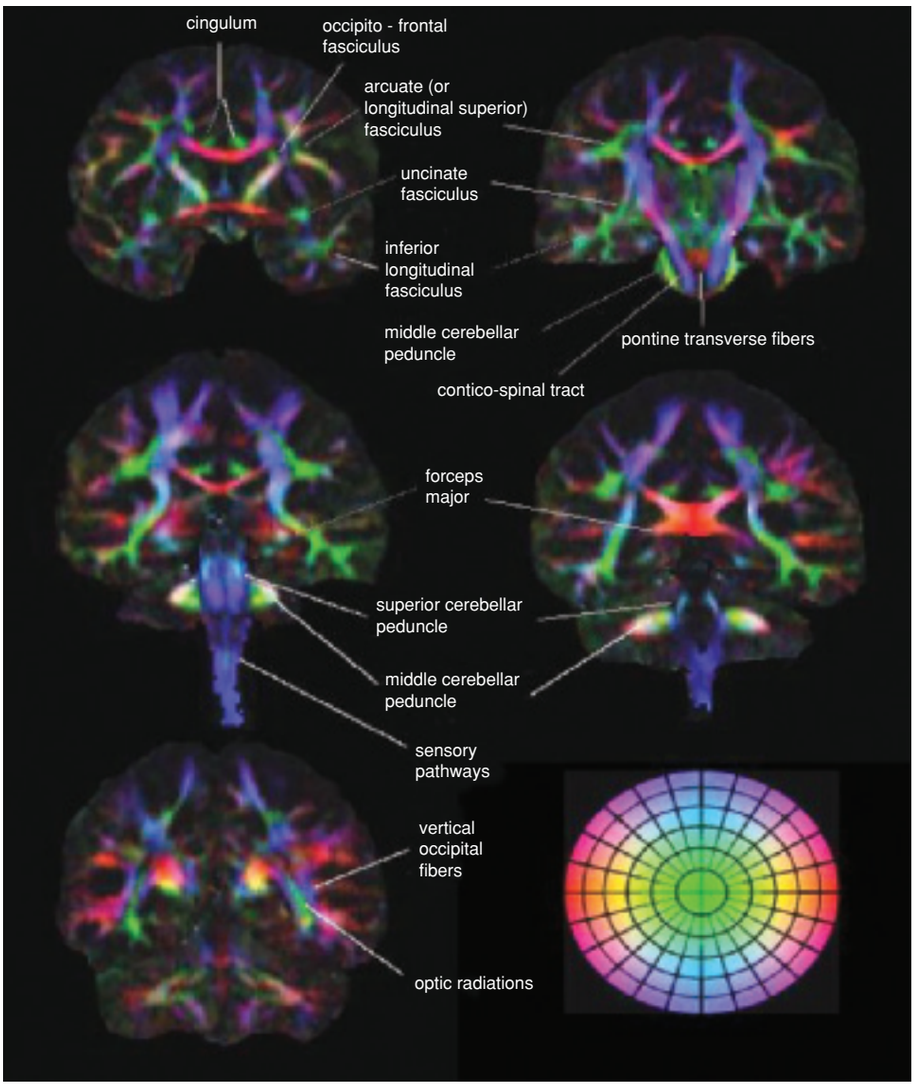

FIGURE 31.11. This direction-encoded color map allows us to identify the major association, commissural, and projection pathways in the brain. (From Pajevic S, Pierpaoli C. Color schemes to represent the orientation of anisotropic tissues from diffusion tensor data: application to white matter fiber tract mapping in the human brain. *Magn Reson Med* 1999;42(3):526–540, with permission.)

DWI Artifacts

Numerous well-known artifacts can affect DW image quality, which are presented here in the order of their importance. Subject motion during the MR scan can cause ghosting or an artifactual redistribution of signal intensities within DWIs. Rigid-body motion, such as rotation and translation, is the easiest to correct for, since it involves applying a uniform phase offset to an entire image. This problem has been addressed by incorporating navigator echoes in the DWI pulse sequence (92,93). More pernicious is non–rigid-body motion caused by eye movements, pulsations of cerebrospinal fluid, and so on. These artifacts have not been completely eliminated, but they can be mitigated by the use of fast echo-planar DWI sequences and cardiac gating.

The large, rapidly switched magnetic field produced by the gradient coils during the diffusion sequence induces eddy currents in the electrically conductive structures of the MRI scanner, which in turn produce an additional unwanted, slowly decaying magnetic field. Two undesirable effects result: (a) The field gradient at the sample differs from the prescribed field gradient (thus causing a deviation from the prescribed b matrix), and (b) the slowly decaying field causes geometrical distortion of the DWI. These artifacts can adversely affect diffusion imaging studies because the diffusion coefficient or diffusion tensor is generally calculated in each voxel from a multiplicity of DWIs assuming that the prescribed gradients are the same as the gradients actually being applied to the tissue. Uncompensated image distortion can lead to systematic errors in these estimated

DTI Fiber Tractography

$$\underline{D}(\mathbf{r}) \Longrightarrow \varepsilon_1(\mathbf{r}) \equiv \mathbf{t}(s)$$

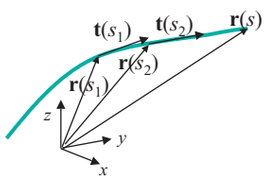

A fiber tract is represented by a *space curve*, $\mathbf{r}(s)$, whose trajectory is found from the diffusion tensor field, $\underline{D}(\mathbf{r})$, by following the direction of maximum diffusivity.

FIGURE 31.12. The central idea in diffusion tensor imaging (DTI) fiber tractography is to follow the direction of maximum diffusivity from some chosen starting point on a fiber. Here, the fiber is depicted in blue. The differential equation used to calculate it is also given (83).

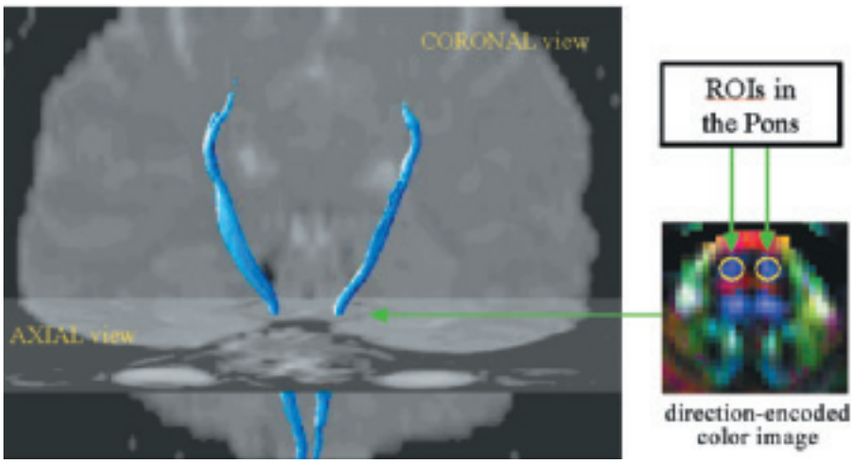

FIGURE 31.13. Examples of computed fiber tracts in the brain, using the scheme outlined in Fig. 31.12. In particular, the pyramidal tracts are reconstructed by launching trajectories in both directions within white matter regions of interest (ROIs) chosen in the Pons (shown on the right).

diffusion parameters. Single-shot echo planar imaging (EPI) acquisitions are quite susceptible to eddy-current artifacts, and so correction schemes have to be used. One widely used strategy is to warp each DWI to a common template; another is to try to use a model of the effects of the eddy current on the phase map to correct it (94). An additional successful approach uses a twice-refocused spin echo sequence (95).

Large discontinuities in the bulk magnetic susceptibility, such as those that occur at tissue–air interfaces, produce local magnetic field gradients that are notorious for their contribution to image distortion, particularly during EPI. In addition to the image distortion, susceptibility variations within the brain adversely affect DWIs because the additional local gradients act like diffusion gradients, causing the *b* matrix to be spatially varying. Fortunately, this affect appears to be limited to the volume of the brain adjacent to the sinuses (96).

Although at low levels of diffusion weighting the logarithm of the signal attenuation decreases linearly with increasing *b* value, background noise causes the DWI intensity to approach a baseline "noise floor" as one progressively increases the degree of diffusion weighting. Noise can introduce errors in the estimated diffusion coefficients or diffusion tensors when using Eq. 6 or 7 in this regime. Background noise leads primarily to a bias in anisotropy measures of $\underline{D}$ because noise always makes isotropic media appear anisotropic and anisotropic media appear more anisotropic (66). It was found that noise can also bias the mean and variance of the eigenvectors of $\underline{D}$ (97). There are few useful remedies to correct for noise (66,97–99).

The following problems can produce artifacts as well: Improper refocusing of radiofrequency pulses leads to additional signal loss. Background gradients can be present because of improper shimming, which leads to additional signal attenuation if not properly compensated for. This problem can often be remedied by measuring the background gradients directly (100) and incorporating them explicitly in the formula relating the signal intensity and the diffusion coefficient or tensor. Flipping the signs of the diffusion gradients on alternate averages has been suggested as an aid in removing most cross-terms. Clearly, cross-terms arising between imaging gradients, albeit small, would not be corrected using this method. Moreover, averaging should be done on the logarithm of the intensity rather than the intensity; otherwise, gradient cancellation will not occur. Gradient nonlinearity and miscalibration can lead to errors in the calculation of the diffusion coefficient or diffusion

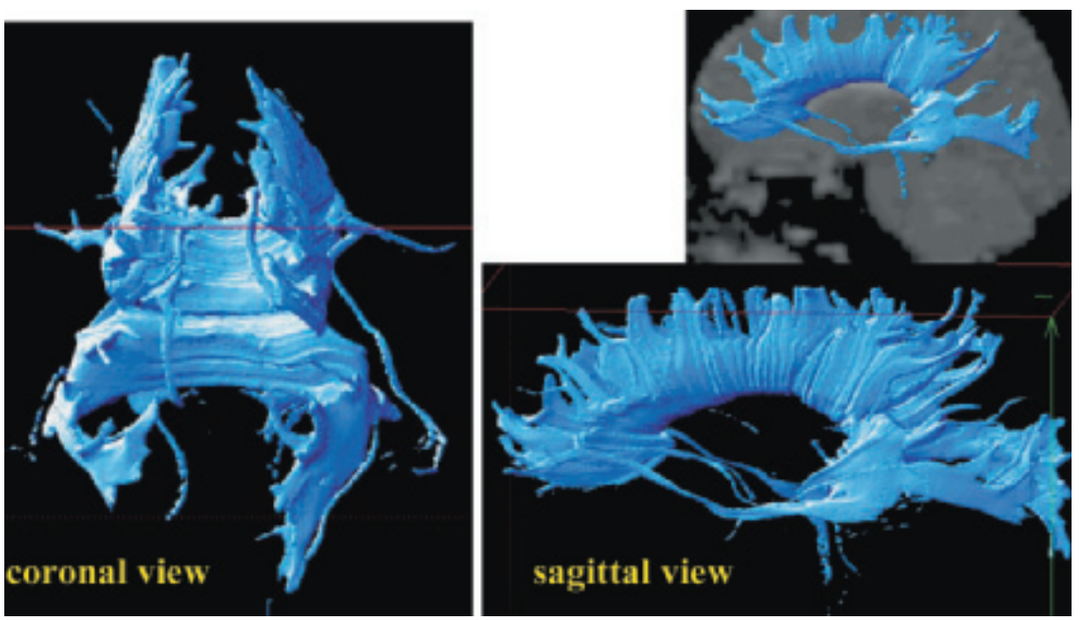

FIGURE 31.14. The corpus callosum is reconstructed by launching fibers in both directions starting from a region of interest located in the interhemispheric plane. Both coronal and sagittal views are shown.

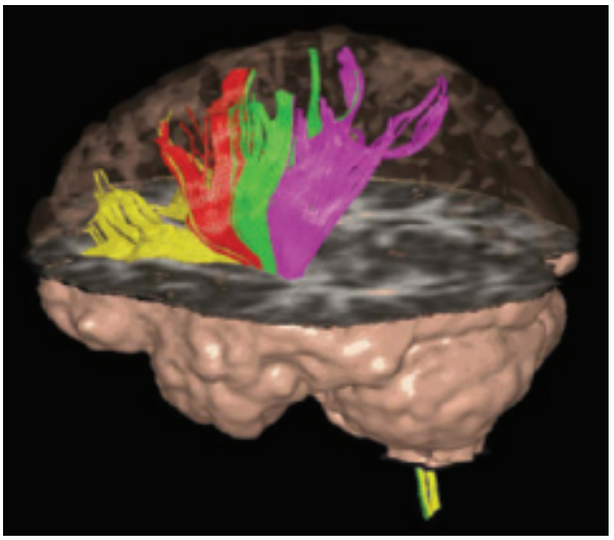

FIGURE 31.15. An example of computed fiber tract trajectories in the human brain. Here, bundles of fascicles are represented as streamtubes whose axes follow the local direction of maximum diffusivity. High-dimensional diffusion tensor imaging data provide information to construct maps of white matter pathways. (Courtesy of Derek Jones.)

tensor from a set of DWIs. The diffusion attenuation at different gradient strengths must be known for these formulas to provide meaningful results. If these gradients are not well calibrated or are not linear, signal attenuation observed in the image will be misattributed to diffusion processes in the sample. If the gradients in the x, y, and z directions are coupled to one another (i.e., there is cross-talk) because of misalignment, then gradients applied in logical directions may have components in other directions. Such cross-talk could lead to problems, particularly in diffusion tensor MRI (101,102).

Problems in Inferring Tissue Microstructure from the NMR Signal

Inferring the microstructure and the underlying architectural organization of tissue using diffusion imaging data is complicated by several factors. First, homogeneity within each voxel cannot be assumed. Numerous microscopic compartments exist in brain parenchyma. Typically gray matter, white matter, and cerebrospinal fluid can occupy the same voxel. Generally, the number of these distinct tissue types and their distribution within the voxel are unknown. At an ultrastructural level, gray matter and white matter are generally quite heterogeneous, having a distribution of macromolecular structures with a range of sizes, shapes, composition, and physical properties (such as T_2, D). Differences in relaxation parameters can lead to different rates of echo attenuation in each compartment, making it more difficult to explain the cause of signal loss within a voxel. There are also irregular boundaries between macromolecular and microscopic-scale compartments. Different macromolecular structures comprising these boundaries may affect the displacement distribution of water molecules differently. Water molecular motion may be restricted or hindered. Some water will be associated with certain macromolecules, whereas some will be free to diffuse. Generally, how water moves within and between tissue compartments is not well understood.

Another unknown is whether there is exchange between compartments, which can also affect the relaxation rates of the spin system. Owing to differences in blood flow and thermal conductivity, temperature cannot be assumed to be uniform throughout a tissue sample. It is well known that temperature affects the measured diffusivity (103–105).

As an aside, the foregoing list explains in part why the underlying cause of diffusion anisotropy has not been fully elucidated in brain parenchyma. Previously, it was thought that ordered, heterogeneous structures, such as large, oriented extracellular and intracellular macromolecules, supermacromolecular structures, organelles, and membranes, all contributed

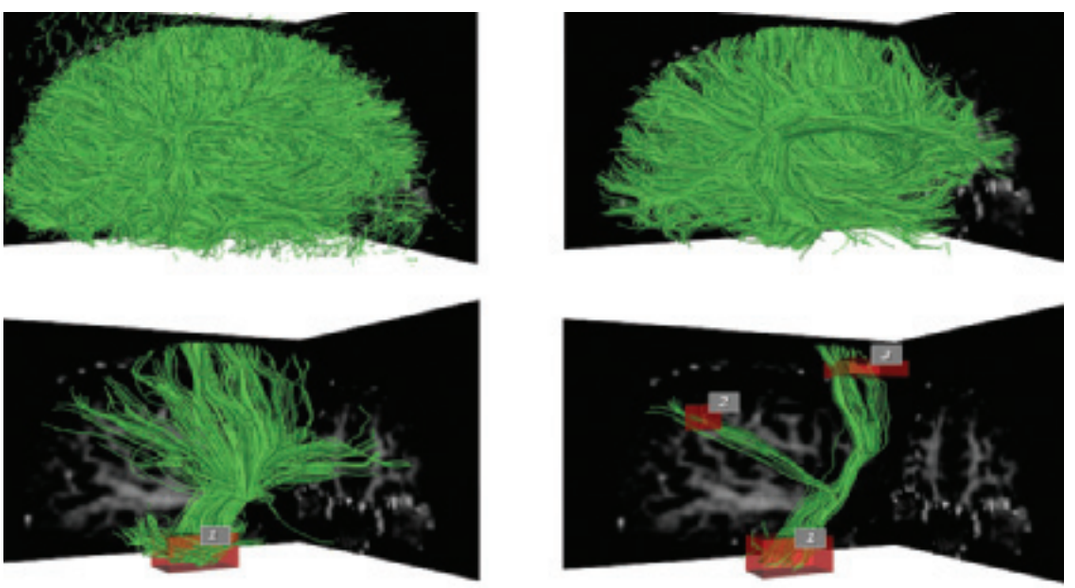

FIGURE 31.16. Connectivity implied by tractography. Lateral surface view (**top left**) and mesial surface view (**top right**) demonstrate the remarkably high density of fiber bundles using an alternative postprocessing algorithm. With this interface, a user-defined voxel of interest in the internal capsule (**bottom left**) segments out bundles, which are further defined to intersect multiple such selected voxels (**bottom right**), potentially indicating functional connectivity. (From Sherbondy A, Akers D, Mackenzie R, et al. Exploring connectivity of the brain's white matter with dynamic queries. *IEEE Trans Vis Comp Graphics* 2005;11:419–430, with permission.)

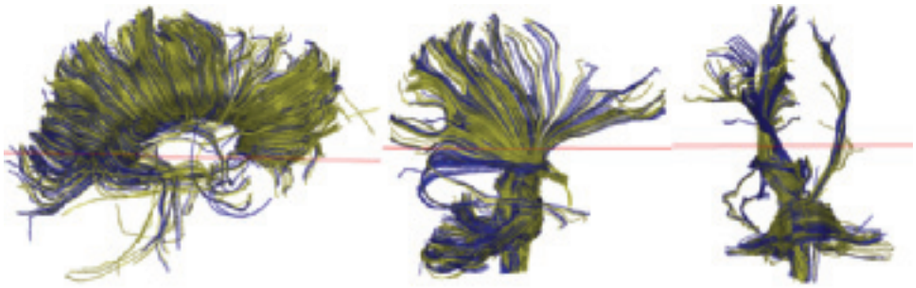

FIGURE 31.17. Dependence of diffusion tensor imaging (DTI) tractography on signal-to-noise ratio (SNR). DTI tractography of fiber bundles in corpus callosum (**left**) and corticospinal tracts (**center, right**) shows significant difference in apparent density of white matter bundles solely based on differing acquisition techniques with SNR. Gold-colored bundles were generated using six excitations, whereas blue-colored bundles were generated using a clinically feasible protocol with one excitation. (Courtesy of R. Bammer, Stanford.)

to diffusion anisotropy (106); however, work by Beaulieu (107,108) implicated nerve membranes as the primary cause of diffusion anisotropy. In the central nervous system, it is clear that diffusion anisotropy is not simply caused by myelin in white matter because it has been shown in several studies that even before myelin is deposited, diffusion anisotropy can be measured using MRI (107–110). Thus, despite the fact that increases in myelin are temporally correlated with increases in diffusion anisotropy, structures other than the myelin sheath must be contributing to diffusion anisotropy. This is an important point because there is a common misconception that the degree of diffusion anisotropy can be used as a quantitative measure or "stain" of myelin content, when, in reality, no such simple relationship exists.

With the advent of stronger magnetic field gradients, several groups have reported multiexponential decay of the MR signal intensity as a function of *b* value (e.g., ref. 111) and have attempted to infer from it the properties of distinct tissue compartments. With only background noise added to the DWI signal, one could misinterpret the noise baseline as arising from a separate compartment. Putting aside the complexities of obtaining stable estimates of discrete exponentials (i.e., diffusion relaxography), numerous microstructural and architectural configurations could produce the same multiexponential relaxation data. For example, Peled et al. showed that a system of impermeable tubes with a distribution of diameters consistent with those found in histologic brain slices could give rise to multiexponential decay of the signal (112). Similar behavior is expected when there is a statistical distribution of any relevant physical property or microstructural dimension within a voxel. It is unlikely that a particular exponential can ever meaningfully be assigned to a particular and distinct tissue compartment. Clearly, without invoking additional a priori information about tissue structure, tissue composition, the physical properties of the different compartments, and their spatial distribution, determining tissue microstructural and architectural features from the NMR signal is an ill-posed and intractable inverse problem.

Multisite or Longitudinal Studies

Longitudinal studies are becoming important in following patients with stroke and neurodegenerative diseases to assess the natural history of diseases and predict outcome (Fig. 31.18). Multisite studies are also becoming increasingly feasible in an era in which DTI has become widely available in the clinic and is being used to explore brain development and a broad array of disease processes in the brain in general. Drug safety and efficacy can also potentially be evaluated by DTI and other quantitative imaging methods. In performing multisite or longitudinal DTI studies, several additional issues arise. The most basic is how to compare high-dimensional diffusion tensor data from different individuals or from the same individual at different times. This tensor data generated from a DTI acquisition contains both scalar and vector information. Applying warping transformations developed only for scalar images produces nonsensical results when applied to DTI data unless one takes appropriate precautions to preserve the features of the tensor field. There is still much work to be done to understand how properly to warp and register diffusion tensor field data.

In both longitudinal and multisite studies, it is advisable to use the same imaging acquisition hardware, reconstruction software, and postprocessing routines to help control for unnecessary variability. All sites should use a well-characterized physical phantom, even if it is an isotropic phantom, to ensure that no systematic artifacts occur and that features of the DWIs are stable in time and among platforms. "Living phantoms" can also be useful for this purpose.

Statistical analysis of diffusion and diffusion tensor imaging data is complicated by several factors. Although in an ideal diffusion tensor imaging experiment, $\underline{D}$ has been shown to be distributed according to a multivariate normal distribution (113) and Trace($\underline{D}$) has been shown to be normally distributed (114), the parametric distribution of many other derived parameters is either unknown or known not to be normal. In these cases, we are precluded from using statistical hypothesis-testing methods that assume an underlying normal distribution to determine whether an observed difference between different regions of interest is statistically significant. Empirical methods like the bootstrap—which allow determination of the distribution of a statistical parameter empirically without knowledge of the form of its distribution a priori—show great promise in diffusion imaging studies (113), particularly now that many single-shot DWIs can be acquired during a single scanning session, making this method practicable and accurate. Statistical properties of measured DTI parameters can then be compared on a voxel-by-voxel basis to assure data quality.

CONCLUSION

Both diffusion MRI and diffusion tensor MRI that subsumes it provide new means to probe tissue structure at different levels of hierarchic organization (Fig. 31.19). Although experimental diffusion times are associated with water molecule displacements on the order of micrometers, these molecular motions are ensemble averaged within a voxel and then subsequently assembled into multislice or 3D images of tissues and organs.

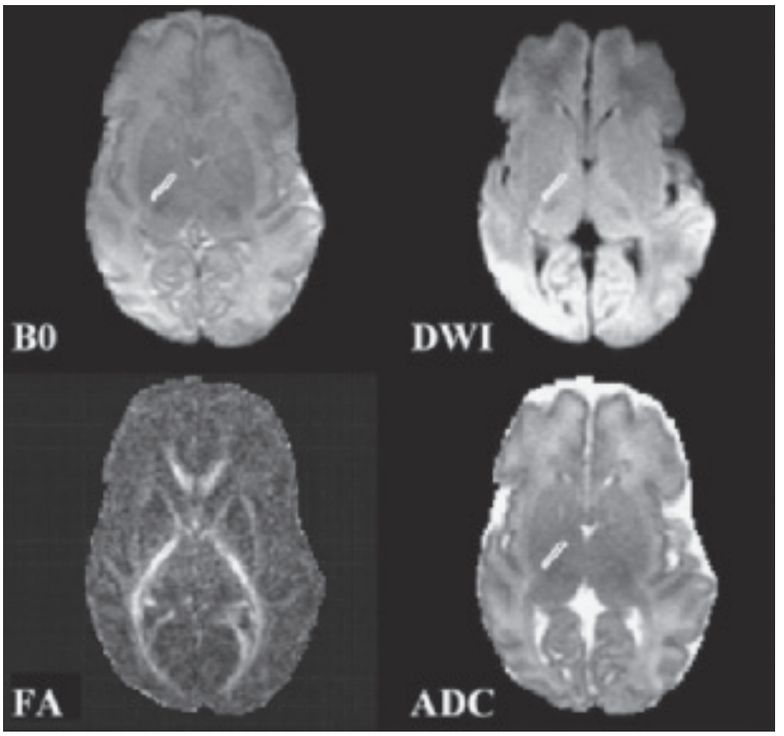

FIGURE 31.18. Prediction of outcome in premature infants by diffusion tensor imaging data. Data from a normal-appearing right internal capsule on T2-weighted imaging (**upper left**), also shown on the corresponding diffusion-weighted image (DWI), fractional anisotropy map (FA), and apparent diffusion coefficient map (ADC), showed a statistically significant abnormality in white matter structure in very low birth weight infants with poor outcome compared with an otherwise similar group of premature infants who had normal neurologic outcome. Magnetic resonance imaging was performed at a term-equivalent age in all individuals. (From Arzoumanian Y, Mirmiran M, Barnes PD, et al. Diffusion tensor brain imaging findings at term-equivalent age may predict neurologic abnormalities in low birth weight preterm infants. *AJNR Am J Neuroradiol* 2003;24: 1646–1653, with permission.)

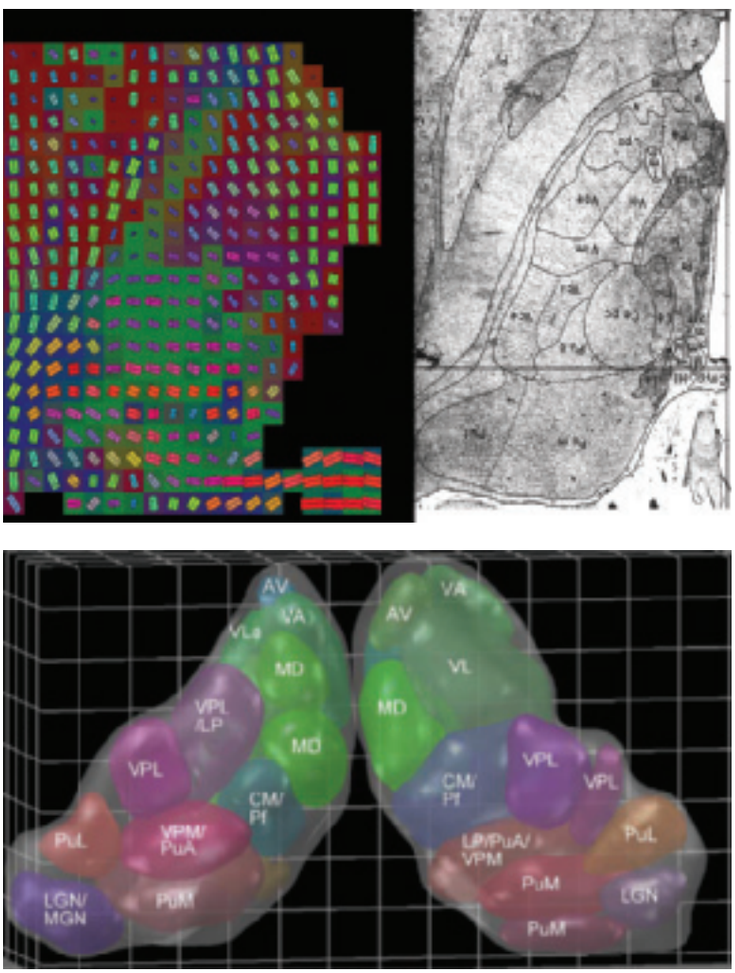

FIGURE 31.19. Segmented anatomy of thalamic nuclei by diffusion tensor imaging. Using an automated segmentation method of postprocessing called the k-means clustering algorithm, an elegant depiction of the nuclei within the thalamus (bottom) is generated from raw diffusion tensor images (top left). The detail of anatomy surpasses traditional textbook depictions of histopathology (top right). (From Wiegell MR, Tuch DS, Larsson HB, et al. Automatic segmentation of thalamic nuclei from diffusion tensor magnetic resonance imaging. *NeuroImage* 2003;19:391–401, with permission.)

Thus, this imaging modality permits us to study and elucidate complex structural and architectural features spanning length scales ranging from the macromolecular to the macroscopic without the use of exogenous contrast agents.

Quantitative parameters derived from the diffusion tensor, such as maps of the eigenvalues of the diffusion tensor, its trace, measures of the degree of diffusion anisotropy and organization, estimates of fiber direction, and fiber tract trajectories, will all help to advance our assessment of the nervous system.

GLOSSARY

Apparent diffusion coefficient (ADC): A diffusion coefficient that is determined, generally, by taking the ratio of the mean-squared displacement measured along a particular direction and the diffusion time of the experiment.
Anisotropic: Not appearing the same in all directions.
Diffusion: A process in which molecules are mixed through the action of random collisions among themselves and with other molecules or structures.
Diffusion anisotropy: A property of diffusion exhibited in some media in which the rate of diffusion is different in different directions.
Diffusion map: An image computed from a series of diffusion-weighted images in which the intensity displayed in each voxel is the computed ADC in that voxel (usually obtained with diffusion gradients applied in a particular direction).
Diffusion tensor map: A set of six images computed from a series of diffusion-weighted images in which the intensity displayed in each voxel represents the value of one of the six independent components of the effective diffusion tensor measured in that voxel.
Diffusion weighting: The process of rendering a NMR echo sensitive to translational diffusion, generally by incorporating diffusion gradients within a spin-echo sequence.
DWI (diffusion-weighted image): An MR image that has been diffusion weighted by the incorporation of diffusion gradients within the imaging sequence.
Fractional anisotropy (FA): A measure of diffusion anisotropy, which represents the ratio of the magnitude of the anisotropic part of the diffusion tensor to the magnitude of the entire diffusion tensor.
Heterogeneous: A property of a material that varies as a function of position, that is, is spatially nonuniform.
Hindered diffusion: A diffusion process in which labeled molecules are able to explore most of the medium but are excluded from a set of isolated subregions or subdomains within the medium.
Homogeneous: A property of a material that appears the same as a function of position, that is, is spatially uniform.
Isotropic: Appearing the same in all directions.
Isotropically weighted MRI: An image computed from a series of diffusion-weighted images in which the intensity is a function of Trace(D).
Relative anisotropy (RA): A measure of diffusion anisotropy, which represents the ratio of the magnitude of the anisotropic part of the diffusion tensor to the magnitude of the isotropic part of the diffusion tensor.
Restricted diffusion: A diffusion process in which labeled molecules are confined to subregions or subdomains within the medium.
Self-diffusion: A process in which molecules are mixed through the action of random collisions among themselves.

ACKNOWLEDGMENTS

Several people deserve special recognition for their contributions to this review and to diffusion imaging in general. Sinisa Pajevic is responsible for implementing methods for approximating tensor fields smoothly, performing parametric and nonparametric statistical analysis of DTI data, and encoding fiber directions using color. He also processed many of the images displayed in this chapter. Carlo Pierpaoli acquired many of the DWIs used here and has been largely responsible for migrating DTI from the bench to the bedside. Akram Aldroubi provided the mathematical underpinnings for a continuous approximation to the discrete tensor data that has made DTI fiber tractography possible. Alan Barnett developed interleaved DW EPI sequences used in most of our clinical studies. Denis LeBihan and Jim Mattiello are coinventors of DTI. Bob Turner developed the first DW EPI sequences on which our subsequent DWI sequences are based. Raisa Freidlin, Guan Koay, and Liz Salak read and edited this chapter.

References

1. Crank J. *The mathematics of diffusion*, 2nd ed. Oxford: Oxford University Press, 1975.
2. Jost W. *Diffusion in solids, liquids, and gases*. New York: Academic Press, 1960.
3. Nicholson C. Quantitative analysis of extracellular space using the method of TMA+ iontophoresis and the issue of TMA+ uptake. *Can J Physiol Pharmacol* 1992;70(Suppl):S314–S322.
4. Nicholson C. Ion-selective microelectrodes and diffusion measurements as tools to explore the brain cell microenvironment. *J Neurosci Meth* 1993;48(3):199–213.
5. Brown R. On the general existence of active molecules in organic and inorganic bodies. *Phil Mag Ann Phil (NS)* 1828:4.
6. Einstein A. Über die von der molekularkinetischen Theorie der Wärme geforderte Bewegung von in ruhenden Flüssigkeiten suspendierten Teilchen. *Ann Phys* 1905;17:549–560.
7. Einstein A. *Investigations on the theory of the Brownian movement*. New York: Dover, 1926.
8. Hahn EL. Spin-echoes. *Phys Rev* 1950;80(4):580–594.
9. Carr HY, Purcell EM. Effects of diffusion on free precession in nuclear magnetic resonance experiments. *Phys Rev* 1954;94(3):630–638.
10. Bloch F. Nuclear induction. *Phys Rev* 1946;70(7/8):460–474.
11. Torrey HC. Bloch equations with diffusion terms. *Phys Rev* 1956;104(3):563–565.
12. Douglass DC, McCall DW. Diffusion in paraffin hydrocarbons. *J Phys Chem* 1958;62:1102.
13. Neuman CH. Spin echo of spins diffusing in a bounded medium. *J Chem Phys* 1974;60(11):4508–4511.
14. Stejskal EO. Use of spin echoes in a pulsed magnetic-field gradient to study restricted diffusion and flow. *J Chem Phys* 1965;43(10):3597–603.
15. Wayne RC, Cotts RM. Nuclear-magnetic-resonance study of self-diffusion in a bounded medium. *Phys Rev* 1966;151(1):264–272.
16. Stejskal EO, Tanner JE. Spin diffusion measurements: spin echoes in the presence of time-dependent field gradient. *J Chem Phys* 1965;42(1):288.
17. McCall DW, Douglass DC, Anderson JE. *Ber Besunges Phys Chem* 1963;67:336.
18. Callaghan PT. *Principles of nuclear magnetic resonance microscopy*. Oxford: Oxford University Press, 1991.
19. Tanner JE. Use of the stimulated echo in NMR diffusion studies. *J Chem Phys* 1970;52(5):2523–2526.
20. Tanner JE. Transient diffusion in system partitioned by permeable barriers. Application to NMR measurements with a pulsed field gradient. *J Chem Phys* 1978;69(4):1748–1754.
21. Price WS, Kuchel PW. Effect of nonrectangular field gradient pulses in the Stejskal and Tanner (diffusion) pulse sequence. *J Magn Reson* 1991;94:133–139.
22. Taylor DG, Bushell MC. The spatial mapping of translational diffusion coefficients by the NMR imaging technique. *Phys Med Biol* 1985;30(4):345–349.
23. Chang DC, Hazlewood CF, Nichols BL, et al. Spin echo studies on cellular water. *Nature* 1972;235(5334):170–171.
24. Chang DC, Rorschach HE, Nichols BL, et al. Implications of diffusion coefficient measurements for the structure of cellular water. *Ann NY Acad Sci* 1973;204: 434–443.
25. Rorschach HE, Chang DC, Hazlewood CF, et al. The diffusion of water in striated muscle. *Ann NY Acad Sci* 1973:444–458.
26. Cooper RL, Chang DB, Young AC, et al. Restricted diffusion in biophysical systems. *Exp Biophys J* 1974;14(3):161–177.
27. Hazlewood CF, Rorschach HE, Lin C. Diffusion of water in tissues and MRI. *Magn Reson Med* 1991;19(2):214–216.
28. Tanner JE. Measurement of self-diffusion in colloid systems by magnetic-field-gradient, spin-echo methods. In: Resing HA, Wade CG, eds. *Magnetic resonance in colloid and interface sciences*. Washington, DC: ACS, 1976:16–30.
29. Tanner JE. Self-diffusion of water in frog muscle. *Biophys J* 1979;28(1):107–116.
30. Cleveland GG, Chang DC, Hazlewood CF, et al. Nuclear magnetic resonance measurement of skeletal muscle: anisotropy of the diffusion coefficient of the intracellular water. *Biophys J* 1976;16(9):1043–1053.
31. Hansen JR. Pulsed NMR study of water mobility in muscle and brain tissue. *Biochim Biophys Acta* 1971;230(3):482–486.
32. LeBihan D, Breton E. Imagerie de diffusion in-vivo par resonance magnetique nucleaire. *C R Acad Sci Paris* 1985;301:1109–1112.
33. Merboldt KD, Hanicke W, Frahm J. Self-diffusion NMR imaging using stimulated echoes. *J Magn Reson* 1985;64:479–486.
34. Wesbey GE, Moseley ME, Ehman RL. Translational molecular self-diffusion in magnetic resonance imaging. II. Measurement of the self-diffusion coefficient. *Invest Radiol* 1984;19(6):491–498.
35. Wesbey GE, Moseley ME, Ehman RL. Translational molecular self-diffusion in magnetic resonance imaging. I. Effects on observed spin-spin relaxation. *Invest Radiol* 1984;19(6):484–490.

36. Hazlewood CF, Chang DC, Nichols BL, et al. Nuclear magnetic resonance transverse relaxation times of water protons in skeletal muscle. *Biophys J* 1974;14(8):583–606.
37. Lauterbur PC. Image formation by induced local interactions: examples employing nuclear magnetic resonance. *Nature* 1973;242:190–191.
38. LeBihan D. Molecular diffusion nuclear magnetic resonance imaging. *Magn Reson Q* 1991;7(1):1–30.
39. LeBihan D, Basser PJ. Molecular diffusion and nuclear magnetic resonance. In: LeBihan D, ed. *Diffusion and perfusion magnetic resonance imaging*. New York: Raven Press, 1995:5–17.
40. Neeman M, Freyer JP, Sillerud LO. Pulsed-gradient spin-echo studies in NMR imaging. Effects of the imaging gradients on the determination of diffusion coefficients. *J Magn Reson* 1990;90:303–312.
41. Basser PJ. Inferring microstructural features and the physiological state of tissues from diffusion-weighted images. *NMR Biomed* 1995;8(7-8):333–344.
42. Garrido L, Wedeen VJ, Kwong KK, et al. Anisotropy of water diffusion in the myocardium of the rat. *Circ Res* 1994;74(5):789–793.
43. Turner R, LeBihan D, Maier J, et al. Echo-planar imaging of intravoxel incoherent motion. *Radiology* 1990;177(2):407–414.
44. Moseley ME, Cohen Y, Kucharczyk J, et al. Diffusion-weighted MR imaging of anisotropic water diffusion in cat central nervous system. *Radiology* 1990; 176(2):439–445.
45. Moseley ME, Kucharczyk J, Asgari HS, et al. Anisotropy in diffusion-weighted MRI. *Magn Reson Med* 1991;19(2):321–326.
46. Henkelman RM, Stanisz GJ, Kim JK, et al. Anisotropy of NMR properties of tissues. *Magn Reson Med* 1994;32(5):592–601.
47. Basser PJ, Mattiello J, LeBihan D. Estimation of the effective self-diffusion tensor from the NMR spin echo. *J Magn Reson* 1994;103(3):247–254.
48. Basser PJ, Mattiello J, LeBihan D. MR diffusion tensor spectroscopy and imaging. *Biophys J* 1994;66(1):259–267.
49. Mattiello J, Basser PJ, LeBihan D. Analytical expression for the b matrix in NMR diffusion imaging and spectroscopy. *J Magn Reson* 1994;A 108:131–141.
50. Mattiello J, Basser PJ, LeBihan D. The b matrix in diffusion tensor echo-planar imaging. *Magn Reson Med* 1997;37(2):292–300.
51. Mattiello J, Basser PJ, LeBihan D. Analytical calculation of the b matrix in diffusion imaging. In: Bihan DL, ed. *Diffusion and perfusion magnetic resonance imaging*. New York: Raven Press, 1995:77–90.
52. Basser PJ, Mattiello J, LeBihan D. Diagonal and off-diagonal components of the self-diffusion tensor: their relation to and estimation from the NMR spin-echo signal [Abstract]. In: *Book of abstracts: 11th Annual Meeting of the Society of Magnetic Resonance in Medicine*. Berkeley, CA: ISMRM, 1992:1222.
53. Jeffreys H. *Cartesian tensors*. Cambridge: Cambridge University Press, 1931.
54. Basser PJ. Testing for and exploiting microstructural symmetry to characterize tissues via diffusion tensor MRI. In: *ISMRM Fourth Scientific Meeting*. New York: ISMRM, 1996:1323.
55. Hsu EW, Mori S. Analytical expressions for the NMR apparent diffusion coefficients in an anisotropic system and a simplified method for determining fiber orientation. *Magn Reson Med* 1995;34(2):194–200.
56. Basser PJ, LeBihan D. Fiber orientation mapping in an anisotropic medium with NMR diffusion spectroscopy [Abstract]. In: *Book of abstracts: 11th Annual Meeting of the Society of Magnetic Resonance in Medicine*. Berkeley, CA: ISMRM, 1992:1221.
57. Basser PJ, Mattiello J, Pierpaoli C, et al. MR diffusion tensor imaging of ischemic brain in vivo. In: *Proceedings of the 16th Annual International Conference of the IEEE Engineering in Medicine and Biology Society*. Baltimore, 1994:566.
58. Kärger J, Pfeifer H, Heink W. Principles and applications of self-diffusion measurements by nuclear magnetic resonance. In: Waugh J, ed. *Advances in magnetic resonance*. New York: Academic Press, 1988:1–89.
59. Moseley ME, Kucharczyk J, Mintorovitch J, et al. Diffusion-weighted MR imaging of acute stroke: correlation with T2-weighted and magnetic susceptibility-enhanced MR imaging in cats. *AJNR Am J Neuroradiol* 1990;11(3):423–429.
60. Moseley ME, Mintorovitch J, Cohen Y, et al. Early detection of ischemic injury: comparison of spectroscopy, diffusion-, T2-, and magnetic susceptibility-weighted MRI in cats. *Acta Neurochir Suppl* (Vienna) 1990;51:207–209.
61. Moseley ME, Cohen Y, Mintorovitch J, et al. Early detection of regional cerebral ischemia in cats: comparison of diffusion- and T2-weighted MRI and spectroscopy. *Magn Reson Med* 1990;14(2):330–346.
62. Warach S, Gaa J, Siewert B, et al. Acute human stroke studied by whole brain echo planar diffusion-weighted magnetic resonance imaging. *Ann Neurol* 1995;37(2):231–241.
63. Warach S, Chien D, Li W, et al. Fast magnetic resonance diffusion-weighted imaging of acute human stroke. *Neurology* 1992;42(9):1717–1723; Erratum, *Neurology* 1992;42(11):2192.
64. Chenevert TL, Brunberg JA, Pipe JG. Anisotropic diffusion in human white matter: demonstration with MR techniques in vivo. *Radiology* 1990;177(2):401–405.
65. Doran M, Hajnal JV, Van Bruggen N, et al. Normal and abnormal white matter tracts shown by MR imaging using directional diffusion weighted sequences. *J Comput Assist Tomogr* 1990;14:865–873.
66. Pierpaoli C, Basser PJ. Toward a quantitative assessment of diffusion anisotropy. *Magn Reson Med* 1996;36(6):893–906; Erratum, *Magn Reson Med* 1997;37(6): 972.
67. Pierpaoli C, Jezzard P, Basser PJ, et al. Diffusion tensor MR imaging of the human brain. *Radiology* 1996;201(3):637.
68. Ulug AM, Beauchamp N, Bryan RN, et al. Absolute quantitation of diffusion constants in human stroke. *Stroke* 1997;28:483–490.
69. van Gelderen P, de Vleeschouwer MHM, DesPres D, et al. Water diffusion and acute stroke. *Magn Reson Med* 1994;31:154–163.
70. Wong EC, Cox RW, Song AW. Optimized isotropic diffusion weighting. *Magn Reson Med* 1995;34(2):139–143.
71. Wong EC, Cox RW. Single-shot imaging with isotropic diffusion weighting. In: *Proceedings of the Second Annual Meeting of the SMR*. San Francisco, 1994:136.
72. Mori S, van Zijl PC. Diffusion weighting by the trace of the diffusion tensor within a single scan. *Magn Reson Med* 1995;33(1):41–52.
73. Basser PJ, Pierpaoli C. Microstructural and physiological features of tissues elucidated by quantitative-diffusion-tensor MRI. *J Magn Reson B* 1996;111(3): 209–219.
74. Sands DE. *Vectors and tensors in crystallography*. Mineola, NY: Dover, 1995.
75. Shimony JS, McKinstry RC, Akbudak E, et al. Quantitative diffusion-tensor anisotropy brain MR imaging: normative human data and anatomic analysis. *Radiology* 1999;212(3):770–784.
76. Westin C-F, Maier S, Khidir B, Wong EC, Cox RW. Single-shot imaging with isotropic diffusion weighting. In: *Image processing for diffusion tensor magnetic resonance imaging*. Cambridge: Springer-Verlag, 1999:441–452.
77. Pajevic S, Pierpaoli C. Color schemes to represent the orientation of anisotropic tissues from diffusion tensor data: application to white matter fiber tract mapping in the human brain. *Magn Reson Med* 1999;42(3):526–540.
78. Wedeen VJ, Davis TL, Lautrup BE, et al. Diffusion anisotropy and white matter tracts. In: *Proceedings of the Second International Conference on Functional Mapping of the Human Brain*. Boston, 1996:146.
79. Wedeen VJ, Davis TL, Weisskoff RM, et al. White matter connectivity explored by MRI. In: *Proceedings of the First International Conference for Functional Mapping of the Human Brain*. Paris, 1995:69.
80. Basser PJ. New histological and physiological stains derived from diffusion-tensor MR images. *Ann NY Acad Sci* 1997;820:123–138.
81. Basser PJ. Fiber-tractography via diffusion tensor MRI (DT-MRI). In: *Proceeding of the 6th Annual Meeting of the ISMRM*. Sydney, Australia, 1998:1226.
82. Basser PJ, Pajevic S, Pierpaoli C, et al. Fiber-tractography in human brain using diffusion tensor MRI (DT-MRI). In: *Proceedings of the 8th Annual Meeting of the ISMRM*. Denver, 2000:784.
83. Basser PJ, Pajevic S, Pierpaoli C, et al. In vivo fiber-tractography in human brain using diffusion tensor MRI (DT-MRI) data. *Magn Reson Med* 2000;44(4): 625–632.
84. Conturo TE, Lori NF, Cull TS, et al. Tracking neuronal fiber pathways in the living human brain. *Proc Natl Acad Sci U S A* 1999;96(18):10422–10427.
85. Jones DK, Williams SCR, Horsfield MA. Full representation of white-matter fibre direction on one map via diffusion tensor analysis. In: *Proceedings of the 5th ISMRM Meeting*. Vancouver, 1997:1743.
86. Mori S, Crain BJ, Chacko VP, et al. Three-dimensional tracking of axonal projections in the brain by magnetic resonance imaging. *Ann Neurol* 1999;45(2):265–269.
87. Poupon C, Clark CA, Frouin V, et al.. Tracking white matter fascicles with diffusion tensor imaging. In: *Proceedings of the 7th Annual Meeting of the ISMRM*. Philadelphia, 1999:325.
88. Poupon C, Mangin J-F, Frouin V, et al. Regularization of MR diffusion tensor maps for tracking brain white matter bundles. In: *Proceedings of MICCAI'98*. New York: Springer-Verlag, 1998:489–498.
89. Behrens TEJ, Jenkinson M, Brady JM, et al. A probabilistic framework for estimating neural connectivity from diffusion weighted MRI. *Proc Int Soc Magn Reson Med* 2002:1142.
90. Parker GJ, Haroon HA, Wheeler-Kingshott CA. A framework for a streamline-based probabilistic index of connectivity (PICo) using a structural interpretation of MRI diffusion measurements. *J Magn Reson Imaging* 2003;18(2):242–254.
91. Pierpaoli C, Barnett A, Virta A, et al. Diffusion MRI of Wallerian degeneration. A new tool to investigate neural connectivity *in vivo*? In: *Proceedings of the 6th Annual Meeting of the ISMRM*. Sydney, Australia, 1998:1247.
92. Anderson AW, Gore JC. Analysis and correction of motion artifacts in diffusion weighted imaging. *Magn Reson Med* 1994;32(3):379–387.
93. Ordidge RJ, Helpern JA, Qing ZX, et al. Correction of motional artifacts in diffusion-weighted MR images using navigator echoes. *Magn Reson Imaging* 1994;12(3):455–460.
94. Jezzard P, Barnett AS, Pierpaoli C. Characterization of and correction for eddy current artifacts in echo planar diffusion imaging. *Magn Reson Med* 1998;39(5): 801–812.
95. Reese TG, Heid O, Weisskoff RM, et al. Reduction of eddy-current-induced distortion in diffusion MRI using a twice-refocused spin echo. *Magn Reson Med* 2003;49(1):177–182.
96. Clark CA, Barker GJ, Tofts PS. An in vivo evaluation of the effects of local magnetic susceptibility-induced gradients on water diffusion measurements in human brain. *J Magn Reson* 1999;141(1):52–61.
97. Basser PJ, Pajevic S. Statistical artifacts in diffusion tensor MRI (DT-MRI) caused by background noise. *Magn Reson Med* 2000;44(1):41–50.
98. Martin KM, Papadakis NG, Huang CL, et al. The reduction of the sorting bias in the eigenvalues of the diffusion tensor. *Magn Reson Imaging* 1999;17(6):893–901.
99. Jones DK, Basser PJ. "Squashing peanuts and smashing pumpkins": how noise distorts diffusion-weighted MR data. *Magn Reson Med* 2004;52(5):979–993.
100. Jara H, Wehrli FW. Determination of background gradients with diffusion MR imaging. *J Magn Reson Imaging* 1994;4(6):787–797.
101. Basser PJ. A sensitive method to calibrate magnetic field gradients using the diffusion tensor. In: *Proceedings of the Third Meeting of the SMR*. Nice, France, 1995:308.
102. Basser PJ, Mattiello J, LeBihan D, inventors; NIH, assignee. Method and system for measuring the diffusion tensor and for diffusion tensor imaging. U.S. patent 5,539,310. July 23, 1996.
103. LeBihan D, Delannoy J, Levin RL. Temperature mapping with MR imaging of molecular diffusion: application to hyperthermia. *Radiology* 1989;171(3): 853–857.
104. Mills R. Self-diffusion in normal and heavy water in the range 1-45°. *J Phys Chem* 1973;77(5):685–688.
105. Simpson JH, Carr HY. Diffusion and nuclear spin relaxation in water. *Phys Rev* 1958;111(5):1201–1202.
106. Basser PJ, Mattiello J, LeBihan D. MR diffusion tensor spectroscopy and imaging. *Biophys J* 1994;66(1):259–267.
107. Beaulieu C, Allen PS. Determinants of anisotropic water diffusion in nerves. *Magn Reson Med* 1994;31(4):394–400.
108. Beaulieu C. The basis of anisotropic water diffusion in the nervous system—a technical review. *NMR Biomed* 2002;15(7-8):435–455.
109. Neil JJ, Shiran SI, McKinstry RC, et al. Normal brain in human newborns: apparent diffusion coefficient and diffusion anisotropy measured by using diffusion tensor MR imaging. *Radiology* 1998;209(1):57–66.
110. Wimberger DM, Roberts TP, Barkovich AJ, et al. Identification of premyelination by diffusion-weighted MRI. *J Comput Assist Tomogr* 1995;19(1): 28–33.
111. Mulkern RV, Gudbjartsson H, Westin CF, et al. Multi-component apparent diffusion coefficients in human brain. *NMR Biomed* 1999;12(1):51–62.
112. Peled S, Cory DG, Raymond SA, et al. Water diffusion, T(2), and compartmentation in frog sciatic nerve. *Magn Reson Med* 1999;42(5):911–918.
113. Pajevic S, Basser PJ. Parametric and non-parametric statistical analysis of DT-MRI data. *J Magn Reson* 2003;161(1):1–14.
114. Basser PJ, Pajevic S. Dealing with uncertainty in DT-MRI Data. *Isr J Chem* 2003;43(1-2):129–144.